Chapter 3

Micromachined Shear Stress Sensors

3.1 Introduction

A fluid flowing past a solid boundary exerts normal and tangential stresses on it. Normal stresses or pressures are readily measured by connecting a small hole on the surface to a pressure sensor or manometer through a tube. The measurement of the tangential or shear stresses at a surface is much more difficult. However, since the information about the variation of the wall shear stress on a surface is often quite useful in analyzing a flow field, especially turbulent flow, numerous methods of measuring the local wall shear stress [1,2] have been developed so far, including the Stanton tube [3], the Preston tube [4], direct measurement using floating elements [5,6], thermal method using heated elements [7,8,9], the sub-layer fence and the electrochemical technique [10]. Among them, the most often used is the thermal method that relates the local wall shear stress and the rate of heat transfer from small thermal elements mounted flush with the surface because it has many advantages over other techniques. For example, it has negligible interference with the flow; the size of the sensor can be as small as a millimeter; the possibility of measuring fluctuations in the wall shear stress as well as the time average makes them particularly attractive for time-varying flows such as turbulent flows [11].

The typical flush-mounted hot film sensors used to measure wall shear stress are thin metal film resistors, mostly platinum and nickel, deposited on flat substrates. Since only the heat lost to the fluid by convection responds to the change of shear stress, it is desirable to thermally isolate the thin film resistor from the substrate. This minimizes the conductive heat loss and improves the sensitivity and frequency response. In the past, the

approach was to use low thermal conductivity materials as the substrates. These include glass, quartz [11,12], and plastic and polyimide films [13,14], with the polyimide film being the best. Reasonably good sensitivity can be obtained when such sensors are used in a fluid with high thermal conductivity such as water. However, they are not as satisfactory for the measurement in low thermal conductivity fluids such as air. The major problems are the low sensitivity, low frequency response and more importantly, their not-yet-well-understood performance at high frequency unsteady turbulence [15,16]. This is all because of the significant and complicated heat conduction loss to the substrates. Theoretically, improvement of sensor performance can be achieved by further reducing the thickness of the substrates. In reality, this alone will not be feasible because extremely thin substrates are difficult to produce using traditional fabrication technology and is not desirable by sensor users. Also, limited by the fabrication technology, the size of traditional hot-film sensors is typically in the millimeter range [5]. This may be tolerable in measuring the mean value of shear stress, but is certainly not acceptable in shear stress imaging with reasonable spatial resolution (i.e. tenths of mm).

There has been some effort to develop micro hot-film sensors using the more advanced Si microfabrication technology [17,18]. The performances of these devices, however, are not as good as the traditional hot-film sensors. In this chapter, we will present a new type of hot-film shear stress sensor with much improved structures and better performance made possible by silicon surface micromachining technology.

3.2 Design And Fabrication

Our new hot-film shear stress sensor has the cross-sectional structure shown in Figure 3.1. It is quite different from a traditional hot-film sensor. As a matter of fact, the structure is much more delicate and complicated. However, it is readily fabricated by using today's surface micromachining technology.

The sensing element, i.e. the thin film polysilicon resistor, is embedded in a silicon nitride diaphragm which sits on a vacuum cavity so that the conduction loss from the

diaphragm to the silicon substrate is minimal even though the cavity is shallow. Since the silicon nitride diaphragm can be very thin and its thermal conductivity is comparable to that of quartz, the thermal isolation of our sensor is much better than any of the traditional hot-film sensors.

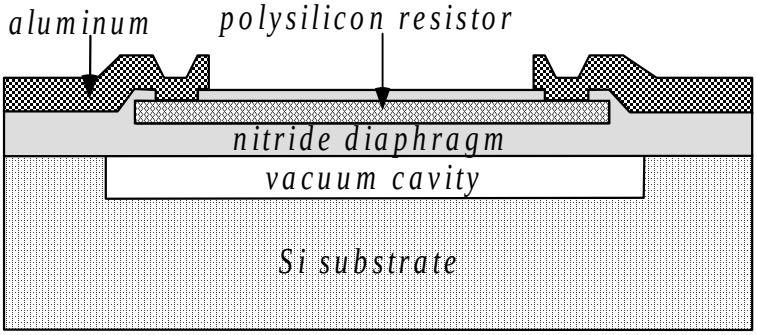

Figure 3.1 Cross-section of the micromachined shear stress sensor.

The design parameters of our sensors include the depth of the vacuum cavity and the dimensions of the diaphragm and polysilicon resistor. The requirement for the aspect ratio of the polysilicon resistor is similar to that of a hot wire sensor, i.e., the resistor has to be long enough to minimize the conduction loss through the ends. On the other hand, it is desirable to have a short polysilicon resistor as it determines the horizontal dimension of the whole sensor. We have decided that a length of 150 μm is a good trade-off. The effect of the width on the sensor performance is not clear at this moment. Therefore, we have designed several sensors with different widths, from 3 μm to 15 μm. The nitride diaphragm has to be slightly larger than the length of the polysilicon resistor to fully accommodate it so we choose 200×200 μm^2. The thickness of the diaphragm is determined to be about 1 μm such that it does not break during fabrication or operation. It can be calculated that the center of a nitride diaphragm with the above dimension will bend approximately 0.8 μm under one atmospheric pressure. Therefore, the depth of the edge of the vacuum cavity should be more than 1 μm to keep the diaphragm from touching the bottom of the cavity.

The fabrication process of the shear stress sensors starts with the deposition of 0.5 μm LPCVD low stress silicon nitride on 4" Si wafers. In the cavity areas, the nitride is removed by plasma etching with a little over-etch to give 0.9 μm trench. Then the wafers are put in oxidation furnace to grow 1.8 μm thick oxide (LOCOS process) in the trench at 1050^{o}C. A short time etch in BHF is performed to planarize the wafers and to remove the oxidized nitride. 0.4 μm of phosphosilicate glass (PSG) is deposited, patterned and annealed to form the sacrificial layer etching channel. Next, 1.2 μm of LPCVD low stress nitride is deposited as the diaphragm material. Etching holes are opened to expose the end of the PSG etching channel, and this is followed by a 49% HF etching to completely remove the PSG and thermal oxide underneath the diaphragm. The cavity is then sealed by LPCVD LTO and nitride deposition at a vacuum of 200 mTorr. The sealing materials on the diaphragm are removed by plasma and BHF etching to minimize the diaphragm thickness. A 0.5 μm polysilicon layer is deposited, doped, annealed and patterned to form the resistors on the diaphragms. Another 0.2 μm of low stress nitride is deposited to passivate the polysilicon resistors. Contact holes are opened through the passivation layer and 1 μm aluminum is evaporated, patterned and sintered to finish the whole process. The fabrication process flow with cross-sections after each step is shown in Figure 3.2 and the SEM picture of a fabricated shear stress sensor is shown in Figure 3.3. The depth of the vacuum cavity on the edges is about 2 μm, which is the sum of the thickness of PSG and thermal oxide remained after planarization. The horizontal dimension of such a sensor is less than 300×300 μm^2, more than four time smaller than the traditional hot-film sensors. The surface roughness is less than 3 μm.

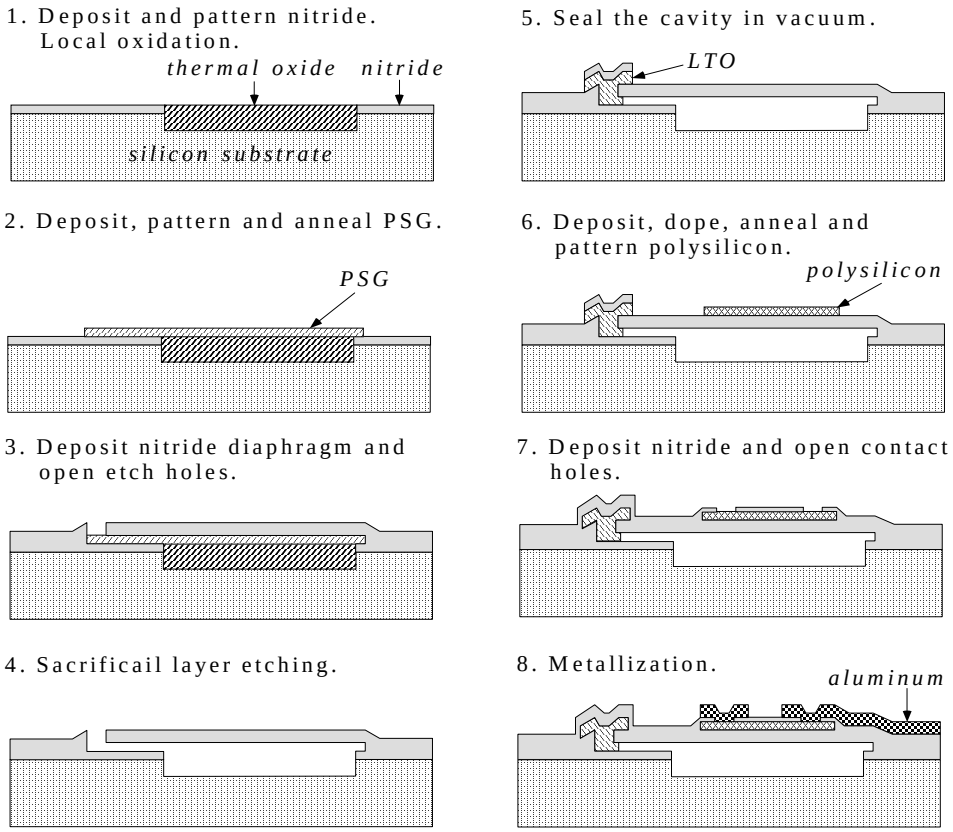

Figure 3.2 Fabrication process flow of the micromachined shear stress sensor.

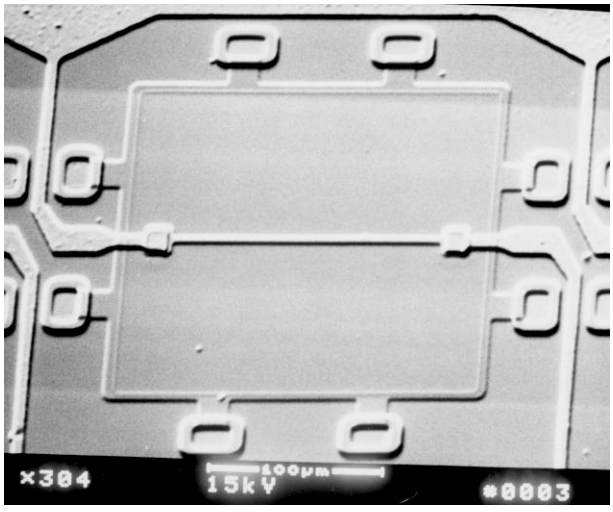

Figure 3.3 SEM picture of a micromachined shear stress sensor. The polysilicon resistor is 150 μm long and 3 μm wide. The nitride diaphragm is 200×200 μm^2. The sensor size is less than 300×300×550 (thickness) μm^3. Note that the entire sensor was in vacuum of the SEM sample chamber so the diaphragm in the picture is flat.

3.3 Heat Transfer Analysis

For the sensor structure shown in Figure 3.4, the heat transfer analysis is rather complicated because strictly speaking, it is a three-dimensional problem. However, it can be simplified to a one-dimensional problem by neglecting the heat conduction in *x* and *z* direction on the diaphragm area (region I) and in *y* and *z* direction on the sensing wire (region II).

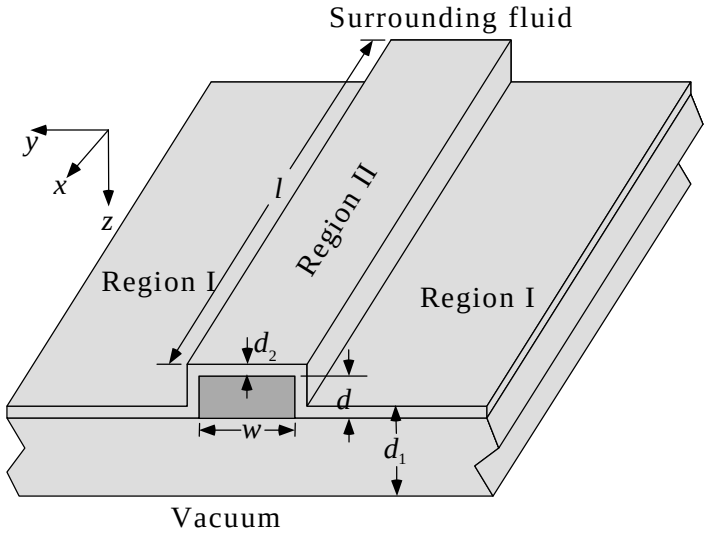

Figure 3.4 Geometry of the diaphragm and the sensing wire.

In an infinitesimal element *dy* in region I ($|y| \geq \frac{w}{2}$), the heat balance equation is

$$(\rho dc_p)_1 ldy \frac{\partial T_1}{\partial t} = \kappa_1 \frac{\partial^2 T_1}{\partial y^2} dyd_1 l - hldy(T_1 - T_a) \tag{3.1}$$

where T_1 is the temperature of the element, T_a is the ambient temperature, *w* and *l* are the width and length of the sensing wire, d_1, κ_1, ρ_1 and c_{p1} are the thickness, thermal conductivity, density and specific heat of the diaphragm, and *h* is the convective heat-transfer coefficient per unit area from the element to the fluid above the diaphragm. Rearranging the above equation yields

$$\frac{1}{\alpha_1}\frac{\partial T_1}{\partial t} = \frac{\partial^2 T_1}{\partial y^2} - \frac{h}{\kappa_1 d_1}(T_1 - T_a) \tag{3.2}$$

where $\alpha_1 = \dfrac{\kappa_1 d_1}{(\rho d c_p)_1}$ is the diffusivity of the diaphragm material. Introducing small perturbations on ambient temperature and heat transfer coefficient, i.e., $T_a = \bar{T}_a + \tilde{T}_a$ and $h = \bar{h} + \tilde{h}$, then

$$T_1 = T_{1s}(y) + T_{1t}(y, t) \tag{3.3}$$

where $T_{1s}(y)$ is the steady-state temperature which satisfies

$$\frac{\partial^2 T_{1s}}{\partial y^2} - \delta^2 (T_{1s} - \bar{T}_a) = 0 \tag{3.4}$$

and $T_{1t}(y, t)$ is the transient temperature change which satisfies

$$\frac{1}{\alpha_1}\frac{\partial T_{1t}}{\partial t} = \frac{\partial^2 T_{1t}}{\partial y^2} - \delta_0{}^2 (T_{1t} - \tilde{T}_a) - \frac{T_{1s} - \bar{T}_a}{\kappa_1 d_1}\tilde{h} \tag{3.5}$$

with $\delta_0 = \sqrt{\dfrac{\bar{h}}{\kappa_1 d_1}}$.

It is easy to show that the solution for Eq. (3.4) with the boundary condition $T_{1s}(\frac{L}{2}) = \bar{T}_a$ is

$$T_{1s} - \bar{T}_a = C_1[e^{-\delta_0 y} - e^{-\delta_0 (L-y)}] \qquad (y \geq \frac{w}{2}) \tag{3.6}$$

where C_1 is the constant of integration. Insert Eq. (3.6) into Eq. (3.5) and perform the Laplace transform,

$$\frac{\partial^2 T_{1t}(y, s)}{\partial y^2} - \left(\delta_0{}^2 + \frac{s}{\alpha_1}\right) T_{1t}(y, s) + \delta_0{}^2 \tilde{T}_a - \frac{C_1\left[e^{-\delta_0 y} - e^{\delta_0 (y-L)}\right]}{\kappa_1 d_1}\tilde{h} = 0 \tag{3.7}$$

The solution for this equation at $y \geq \frac{w}{2}$ with the boundary condition $T_{1t}(\frac{L}{2}) = \frac{\tilde{\tilde{T}}_a}{1+sM_s}$ is

$$T_{1t}(y,s) = \left\{\frac{\delta_0{}^2}{\delta^2}\left[1 - e^{\delta(y-\frac{L}{2})}\right] + \frac{1}{1+sM_s}e^{\delta(y-\frac{L}{2})}\right\}\tilde{T}_a - \frac{\alpha_1}{s\kappa_1 d_1}\tilde{h}C_1\left[e^{-\delta_0 y} - e^{\delta_0(y-L)}\right] + C_2(s)\left[e^{-\delta y} - e^{\delta(y-L)}\right] \quad (3.8)$$

where M_s is the thermal time constant of the substrate and $\delta = \sqrt{\delta_0{}^2 + \frac{s}{\alpha_1}}$.

In region II, the heat balance equation for an infinitesimal dx is

$$(\rho dc_p)_e w dx \frac{\partial T}{\partial t} = \frac{I^2\rho_0}{wd}dx[1+\alpha_R(T-T_0)] + 2(\kappa d)_e dx \left.\frac{\partial T}{\partial y}\right|_{y=\frac{w}{2}} + (\kappa d)_e w dx \frac{\partial^2 T}{\partial x^2} - h(w+2d+2d_2)dx(T-T_a) \quad (3.9)$$

where T_0 is the reference temperature, ρ_0 and α_R are the resistivity and its temperature coefficient of the sensing wire at T_0, $(\rho dc_p)_e = (\rho dc_p)_1 + \rho dc_p$ and $(\kappa d)_e = (\kappa d)_1 + \kappa d$. Rearrange the above equation to get

$$\frac{1}{\alpha_e}\frac{\partial T}{\partial t} = \frac{I^2\rho_0}{(\kappa d)_e w^2 d}[1+\alpha_R(T-T_0)] + \frac{2}{w}\left.\frac{\partial T}{\partial y}\right|_{y=\frac{w}{2}} + \frac{\partial^2 T}{\partial x^2} - \frac{h(w+2d+2d_2)}{(\kappa d)_e w}(T-T_a) \quad (3.10)$$

where $\alpha_e = \frac{(\kappa d)_e}{(\rho dc_p)_e}$ is the effective diffusivity of region II.

In steady state, the above equation becomes

$$\frac{\partial^2 T_s}{\partial x^2} + \frac{\bar{I}^2\rho_0}{(\kappa d)_e w^2 d}[1+\alpha_R(T_s-T_0)] + \frac{2}{w}\left.\frac{\partial T_s}{\partial y}\right|_{y=\frac{w}{2}} - \frac{h(w+2d+2d_2)}{(\kappa d)_e w}(T_s - \bar{T}_a) = 0 \quad (3.11)$$

At $y = \frac{w}{2}$, we have the following boundary conditions

$$T_s = T_{1s}(\frac{w}{2}) \tag{3.12}$$

and

$$(\kappa d)_e \left.\frac{\partial T_s}{\partial y}\right|_{y=\frac{w}{2}} = \kappa_1 d_1 \left.\frac{\partial T_{1s}}{\partial y}\right|_{y=\frac{w}{2}} = -\kappa_1 d_1 \delta_0 C_1 \left[e^{-\delta_0 \frac{w}{2}} + e^{\delta_0 (\frac{w}{2} - L)} \right] \tag{3.13}$$

From Eqs. (3.6) and (3.12), we have

$$C_1 = \frac{T_s - \overline{T}_a}{e^{-\delta_0 \frac{w}{2}} - e^{\delta_0 (\frac{w}{2} - L)}} \tag{3.14}$$

Plug it into Eq. (3.13)

$$\left.\frac{\partial T_s}{\partial y}\right|_{y=\frac{w}{2}} = -\frac{\kappa_1 d_1}{(\kappa d)_e} \frac{\delta_0 (T_s - \overline{T}_a)}{\tanh(\delta_0 L')} \tag{3.15}$$

with $L' = \frac{L - w}{2}$. By substituting the above expression into Eq. (3.11), we can rewrite it as

$$\frac{\partial^2 T_s}{\partial x^2} - \lambda_0{}^2 (T_s - \overline{T}_a - \varepsilon) = 0 \tag{3.16}$$

with

$$\lambda_0{}^2 = \frac{1}{(\kappa d)_e w} \left[\overline{h}(w + 2d + 2d_2) + \frac{2\sqrt{\overline{h}\kappa_1 d_1}}{\tanh(\delta_0 L')} - \frac{\alpha_R \overline{I}^2 R_0}{l} \right] \tag{3.17}$$

$$\varepsilon = \frac{\overline{I}^2 \overline{R}_a}{\lambda_0{}^2 (\kappa d)_e w l} \tag{3.18}$$

and

$$\bar{R}_a = \rho_0 \frac{l}{wd}[1 + \alpha_R(\bar{T}_a - T_0)] = R_0[1 + \alpha_R(\bar{T}_a - T_0)] \tag{3.19}$$

This second-order differential equation can be solved by considering the symmetry of the temperature distribution $T_s(x)$ with respect to $x = 0$ and the boundary condition $T_s(\pm\frac{l}{2}) = \bar{T}_a$. The solution is

$$T_s - \bar{T}_a = \varepsilon - \varepsilon \frac{\cosh(\lambda_0 x)}{\cosh(\lambda_0 l/2)} \tag{3.20}$$

The average temperature increase of the sensing element above the ambient is

$$\bar{T}_s - \bar{T}_a = \varepsilon\left[1 - \frac{2}{\lambda_0 l}\tanh\left(\frac{\lambda_0 l}{2}\right)\right] = \frac{\bar{I}^2 \bar{R}_a}{{\lambda_0}^2 (\kappa d)_e wl}\left[1 - \frac{2}{\lambda_0 l}\tanh\left(\frac{\lambda_0 l}{2}\right)\right] \tag{3.21}$$

Once again, introduce small perturbations on electrical current, ambient temperature and heat transfer coefficient in region II, i.e., $I = \bar{I} + \tilde{i}$, $T_a = \bar{T}_a + \tilde{T}_a$ and $h = \bar{h} + \tilde{h}$, which results in $T = T_s + T_t(t)$. Eq. (3.10) then becomes

$$\begin{aligned} \frac{1}{\alpha_e}\frac{\partial T_t}{\partial t} &= \frac{\bar{I}^2 R_0 \alpha_R T_t + 2\bar{I}\tilde{i} R_0[1 + \alpha_R(T_s - T_0)]}{(\kappa d)_e wl} + \frac{2}{w}\left.\frac{\partial T_t}{\partial y}\right|_{y=\frac{w}{2}} \\ &+ \frac{\partial^2 T_t}{\partial x^2} - \frac{w + 2d + 2d_2}{(\kappa d)_e w}\bar{h}(T_t - \tilde{T}_a) - \frac{w + 2d + 2d_2}{(\kappa d)_e w}(T_s - \bar{T}_a)\tilde{h} \end{aligned} \tag{3.22}$$

The first boundary condition for T_t is

$$T_t = T_{1t}(\frac{w}{2}) \tag{3.23}$$

$$T_t = \left[\frac{{\delta_0}^2}{\delta^2}(1 - e^{-\delta L'}) + \frac{e^{-\delta L'}}{1 + sM_s}\right]\tilde{T}_a - \frac{\alpha_1}{s\kappa_1 d_1}\tilde{h}(T_s - \bar{T}_a) + C_2(s)\left[e^{-\delta\frac{w}{2}} - e^{\delta(\frac{w}{2} - L)}\right] \tag{3.24}$$

$$C_2(s) = \frac{-\left[\frac{\delta_0{}^2}{\delta^2}(1-e^{-\delta L'}) + \frac{e^{-\delta L'}}{1+sM_s}\right]\tilde{T}_a + T_t + \frac{\alpha_1}{s\kappa_1 d_1}\tilde{h}(T_s - \bar{T}_a)}{e^{-\delta\frac{w}{2}} - e^{\delta(\frac{w}{2}-L)}} \tag{3.25}$$

The second boundary condition is

$$\left.\frac{\partial T_t}{\partial y}\right|_{y=\frac{w}{2}} = \frac{\kappa_1 d_1}{(\kappa d)_e}\left.\frac{\partial T_{1t}}{\partial y}\right|_{y=\frac{w}{2}} = \frac{\kappa_1 d_1}{(\kappa d)_e}\left[\frac{1}{1+sM_s}\frac{\delta}{\sinh(\delta L')} + \frac{\delta_0{}^2}{\delta}\tanh\left(\frac{\delta L'}{2}\right)\right]\tilde{T}_a$$
$$-\left[\frac{\delta}{\tanh(\delta L')} - \frac{\delta_0}{\tanh(\delta_0 L')}\right]\frac{\alpha_1\tilde{h}}{s(\kappa d)_e}(T_s - \bar{T}_a) - \frac{\kappa_1 d_1}{(\kappa d)_e}\frac{\delta T_t}{\tanh(\delta L')} \tag{3.26}$$

Insert the above expression into Eq. (3.22) and perform the Lapalace transform

$$\frac{\partial^2 T_t}{\partial x^2} - \lambda^2 T_t + \frac{\upsilon + \sigma}{(\kappa d)_e w} - \frac{\sigma}{(\kappa d)_e w}\frac{\cosh(\lambda_0 x)}{\cosh(\lambda_0 l/2)} = 0 \tag{3.27}$$

with

$$\lambda^2 = \frac{1}{(\kappa d)_e w}\left[\bar{h}(w + 2d + 2d_2) + \frac{2\kappa_1 d_1\delta}{\tanh(\delta L')} - \frac{\alpha_R \bar{I}^2 R_0}{l}\right] + \frac{s}{\alpha_e}$$
$$\approx \lambda_0{}^2\left[1 + b\left(\sqrt{1+\frac{if}{f_1}} - 1\right) + \frac{if}{f_2}\right] \tag{3.28}$$

where $b = \frac{2\sqrt{\bar{h}\kappa_1 d_1}}{\lambda_0{}^2(\kappa d)_e w}$, $f_1 = \frac{\bar{h}\alpha_1}{2\pi\kappa_1 d_1}$ and $f_2 = \frac{\lambda_0{}^2\alpha_e}{2\pi}$. The approximation is valid if $\delta L' > 2$.

$$\upsilon = \left[\bar{h}(w + 2d + 2d_2) + \frac{1}{1+sM_s}\frac{2\kappa_1 d_1\delta}{\sinh(\delta L')} + \frac{2\bar{h}}{\delta}\tanh\left(\frac{\delta L'}{2}\right)\right]\tilde{T}_a + \frac{2\bar{I}\tilde{i}\bar{R}_a}{l} \tag{3.29}$$

$$\sigma = \varepsilon\left\{\frac{2\bar{I}\tilde{i}R_0\alpha_R}{l} - (w + 2d + 2d_2)\tilde{h} - \left[\frac{\delta}{\tanh(\delta L')} - \frac{\delta_0}{\tanh(\delta_0 L')}\right]\frac{2\alpha_1\tilde{h}}{s}\right\} \tag{3.30}$$

The above differential equation can be solved with the help of the boundary condition

$T_t(\pm\frac{l}{2}) = \frac{\tilde{T}_a}{1+sM_s}$ and symmetry $T_t(-x) = T_t(x)$. The solution is

$$T_t = \frac{1}{(\kappa d)_e w}\left\{\begin{array}{l} \dfrac{\upsilon+\sigma}{\lambda^2} - \dfrac{\sigma}{\lambda^2 - {\lambda_0}^2}\dfrac{\cosh(\lambda_0 x)}{\cosh(\lambda_0 l/2)} \\ + \left[\dfrac{\sigma}{\lambda^2 - {\lambda_0}^2} - \dfrac{\upsilon+\sigma}{\lambda^2} + \dfrac{(\kappa d)_e w}{1+sM_s}\tilde{T}_a\right]\dfrac{\cosh(\lambda x)}{\cosh(\lambda l/2)} \end{array}\right\} \tag{3.31}$$

The average temperature fluctuation on the sensing element is

$$\begin{aligned} \bar{T}_t &= \frac{1}{1+sM_s}\frac{2}{\lambda l}\tanh\left(\frac{\lambda l}{2}\right)\tilde{T}_a \\ &+ \frac{1}{(\kappa d)_e w}\left\{\frac{\upsilon+\sigma}{\lambda^2}\left[1-\frac{2}{\lambda l}\tanh\left(\frac{\lambda l}{2}\right)\right] - \frac{\sigma}{\lambda^2-{\lambda_0}^2}\left[\frac{2}{\lambda_0 l}\tanh\left(\frac{\lambda_0 l}{2}\right) - \frac{2}{\lambda l}\tanh\left(\frac{\lambda l}{2}\right)\right]\right\} \end{aligned} \tag{3.32}$$

The resulting sensor resistance change is

$$\Delta R(s) = \alpha_R \bar{T}_t R_0 = r_b(s)\frac{\tilde{i}}{\bar{I}} + G_h(s)\frac{\tilde{h}}{\bar{I}} + G_T(s)\frac{\tilde{T}_a}{\bar{I}} \tag{3.33}$$

and the sensor voltage change is

$$v(s) = \bar{I}\Delta R(s) + \tilde{i}\bar{R} = [r_b(s) + \bar{R}]\tilde{i} + G_h(s)\tilde{h} + G_T(s)\tilde{T}_a \tag{3.34}$$

where

$$r_b(s) = \frac{2\alpha_R \bar{I}^2 {R_0}^2}{{\lambda_0}^2(\kappa d)_e wl}\left\{\begin{array}{l} \dfrac{1+\alpha_R(\varepsilon+\bar{T}_a - T_0)}{(\lambda/\lambda_0)^2}\left[1-\dfrac{2}{\lambda l}\tanh\left(\dfrac{\lambda l}{2}\right)\right] \\ - \dfrac{\alpha_R \varepsilon}{(\lambda/\lambda_0)^2 - 1}\dfrac{2}{\lambda_0 l}\left[\tanh\left(\dfrac{\lambda_0 l}{2}\right) - \dfrac{\lambda_0}{\lambda}\tanh\left(\dfrac{\lambda l}{2}\right)\right] \end{array}\right\} \tag{3.35}$$

is the difference between the ac and dc resistance of the sensor,

$$\begin{aligned} G_h(s) = -\frac{\alpha_R \varepsilon \bar{I} R_0}{{\lambda_0}^2(\kappa d)_e}&\left\{\frac{{\lambda_0}^2}{\lambda^2}\left[1-\frac{2}{\lambda l}\tanh\left(\frac{\lambda l}{2}\right)\right] - \frac{1}{(\lambda/\lambda_0)^2-1}\frac{2}{\lambda_0 l}\left[\tanh\left(\frac{\lambda_0 l}{2}\right) - \frac{\lambda_0}{\lambda}\tanh\left(\frac{\lambda l}{2}\right)\right]\right\} \\ &\left\{1 + \frac{2d+2d_2}{w} + \left[\frac{\delta}{\tanh(\delta L')} - \frac{\delta_0}{\tanh(\delta_0 L')}\right]\frac{2\alpha_1}{sw}\right\} \end{aligned} \tag{3.36}$$

is the ac voltage sensitivity to heat transfer coefficient, and

$$G_T(s) = \frac{\alpha_R \bar{I} R_0}{1 + sM_s} \frac{2}{\lambda l} \tanh\left(\frac{\lambda l}{2}\right) + \frac{\alpha_R \bar{I} R_0}{\lambda^2 (\kappa d)_e w} \left[1 - \frac{2}{\lambda l} \tanh\left(\frac{\lambda l}{2}\right)\right] \left[\bar{h}(w + 2d + 2d_2) + \frac{1}{1 + sM_s} \frac{2\kappa_1 d_1 \delta}{\sinh(\delta L')} + \frac{2\bar{h}}{\delta} \tanh\left(\frac{\delta L'}{2}\right)\right] \tag{3.37}$$

is the ac voltage sensitivity to ambient temperature fluctuation. The first term in Eq. (3.34) represents the voltage drop on a impedance, while the second and third terms represent controlled ac voltage sources. Figure 3.5 shows the equivalent circuit of the sensor.

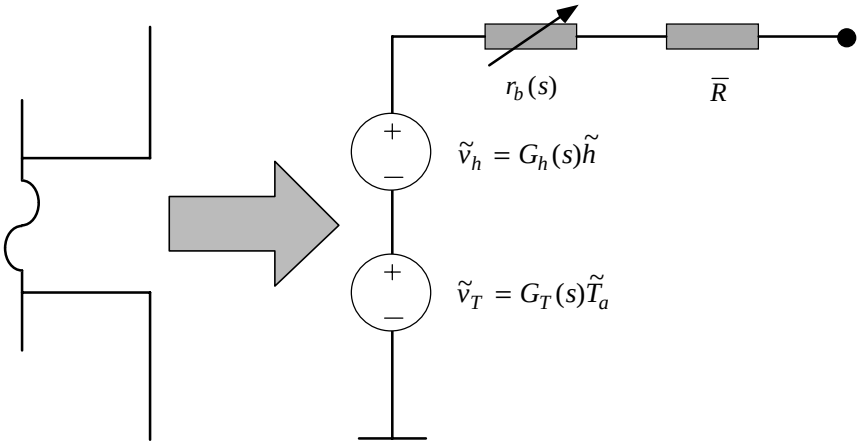

Figure 3.5 (a) Symbol of the shear stress sensor. (b) Equivalent ac circuit model.

3.4 Calibration and Analysis

3.4.1 *I-V* Measurement

The steady-state voltage drop on the sensor is

$$\bar{V} = \bar{I} R_0 [1 + \alpha_R (\bar{T}_s - T_0)] = \bar{I} \bar{R}_a \left\{1 + \frac{\alpha_R \bar{I}^2 R_0}{{\lambda_0}^2 (\kappa d)_e wl} \left[1 - \frac{2}{\lambda_0 l} \tanh\left(\frac{\lambda_0 l}{2}\right)\right]\right\} \tag{3.38}$$

The over-heat ratio of the sensor can be expressed as

$$a_R = \frac{\alpha_R \bar{I}^2 R_0}{\lambda_0{}^2 (\kappa d)_e wl}\left[1 - \frac{2}{\lambda_0 l}\tanh\left(\frac{\lambda_0 l}{2}\right)\right] \tag{3.39}$$

For the micromachined shear stress sensors, polycrystalline silicon is used as the sensing wire material and low stress silicon nitride as the diaphragm material. The resistance - temperature relationship of the sensors are calibrated. The results (Figure 3.6) show a 2.5% non-linearity over a temperature range of 200°C. The above derivations are still valid if α_R is replaced by the average resistance coefficient of temperature (~ 0.11%/°C) extrapolated from the fit to the data in Figure 3.6.

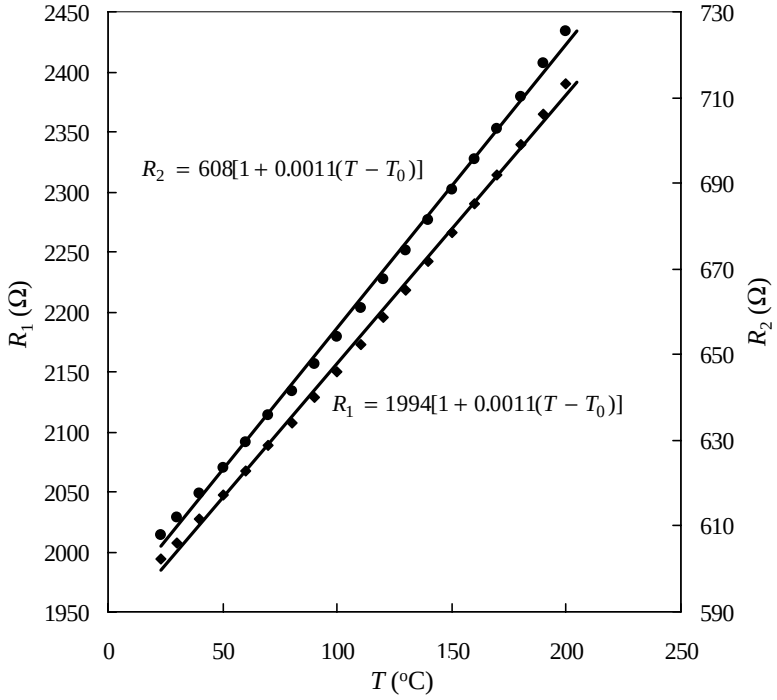

Figure 3.6 The measured resistance-temperature relationships of two boron-doped polysilicon resistors with doping concentration of 2×10^{20} cm^{-3}.

The other physical properties of polysilicon and silicon nitride can be found from various literature. They are: $\rho_0 = 1\times10^{-3}$ Ω·cm, $\kappa = 0.3$ W/cm·°C, $c_p = 0.7$ J/g·°C, $\rho = 2.32$ g/cm^3, $\kappa_1 = 0.032$ W/cm·°C, $c_{p1} = 0.7$ J/g·°C, $\rho_1 = 3.0$ g/cm^3, and $\alpha_1 = 0.015$ cm^2/s. The

dimensions of the sensor structure are: d = 0.55 μm, l = 150 μm, L = 210 μm, d_1 = 1.4 μm, d_2 = 0.2 μm. Then we have $(\kappa d)_e = 2.1\times10^{-5}$ W/°C, α_e = 0.0547 cm^2/s. After fitting Eq. (3.38) and Eq. (3.39) to the *I*-*V* data measured in still air at $T_a = T_0 = 22\,^{o}$C for sensors with different widths (Figure 3.7 and Figure 3.8), we found that the average value of $\bar{h}$ is 0.262 W/cm^2·°C. Note that the convective heat transfer coefficient is non-zero even in still air because there exists the natural or free convection. By using this value of $\bar{h}$, all the parameters in the above equations are calculated and listed in Tables 3.1 and 3.2 for $T - T_a = 100\,^{o}$C.

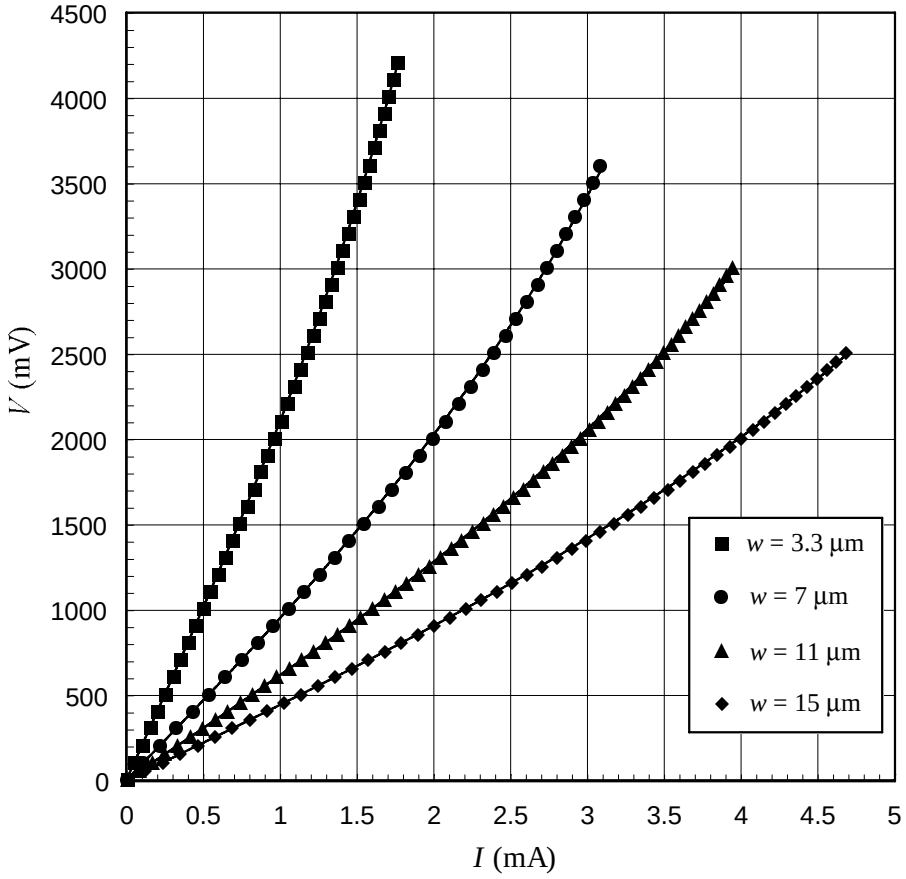

Figure 3.7 Measured *V*-*I* curves (symbols) of the sensors with different widths together with the fitted curves (solid lines) of Eq. (3.38).

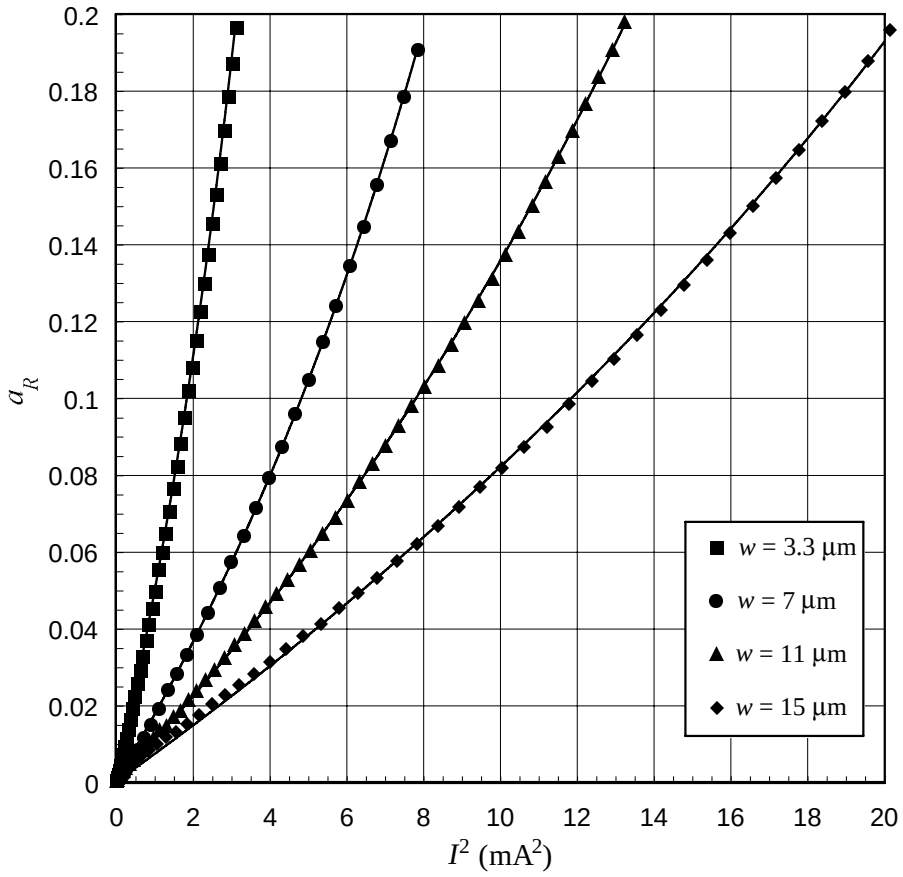

Figure 3.8 The over-heat ratio of the sensors calculated from the measured *I-V* data are plotted against the square of the heating current. The solid lines are the fitted curves of Eq. (3.39).The fitting parameter $\bar{h}$ is found to be 0.262.

Table 3.1 Parameters calculated from measured *I-V* curves.

w (μm)	R_a (Ω)	V (mV)	I (mA)	λ (cm^{-1})	$\alpha_R\varepsilon$	$\lambda l/2$	$\delta L'$
3.3	1994	2976	1.357	516.2	0.1348	3.872	2.491
7	930	2249	2.198	351.5	0.1601	2.636	2.455
11	608	1872	2.799	288.1	0.1820	2.161	2.406
15	438	1665	3.455	252.2	0.2020	1.892	2.358

The temperature distribution on the diaphragm of the sensors can be calculated by using Eqs. (3.6), (3.14) and (3.21). Figure 3.9 shows the contour plot of the 3.3 μm wide

sensor at an over-heat ratio of 0.1. However, it needs to be verified by experimental measurement such as infrared thermal imaging.

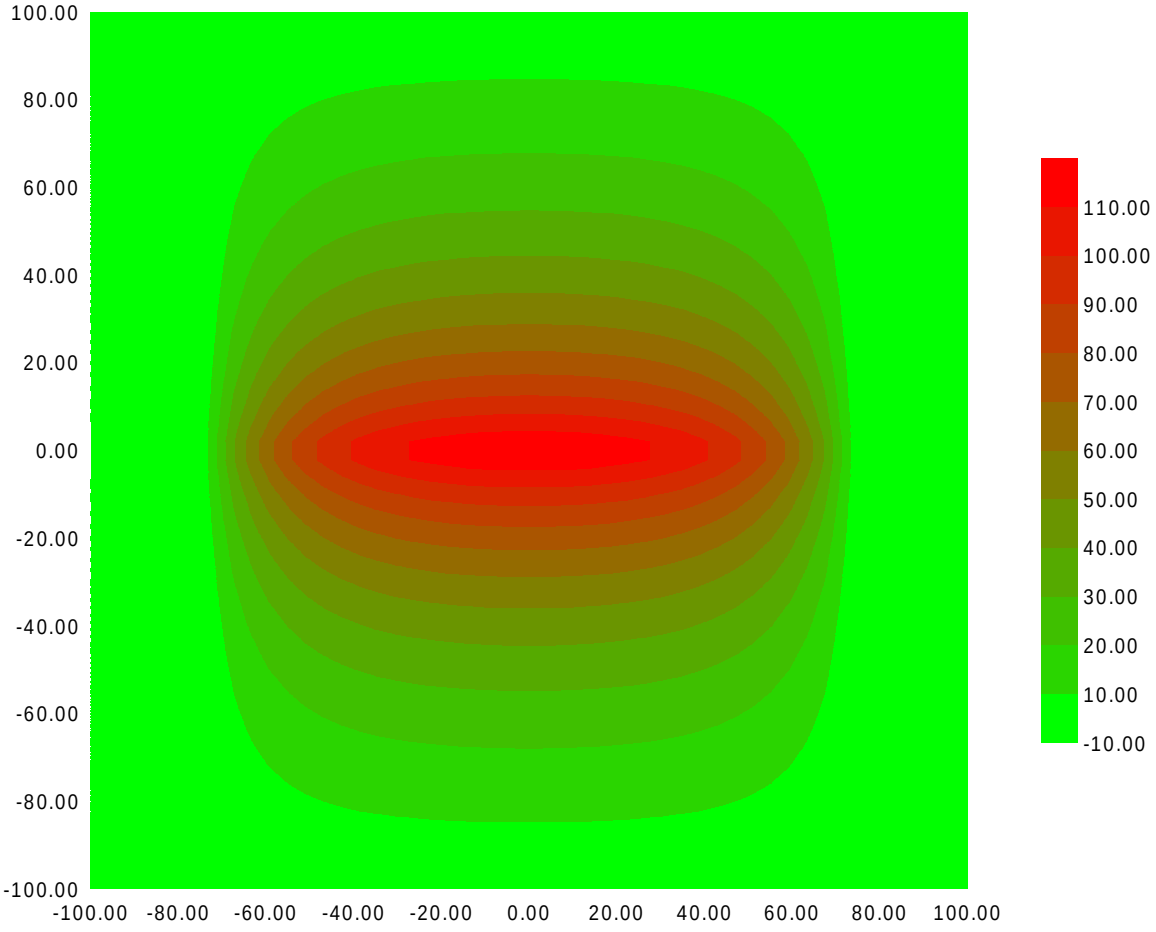

Figure 3.9 Calculated temperature distribution (relative to room temperature) on the diaphragm of the 3.3 μm wide sensor at an over-heat ratio of 0.1.

3.4.2 Temperature Sensitivity

In constant current (CC) mode, when $\overline{h}$ is kept constant, the only parameter in Eq. (3.38) that changes with ambient temperature $\overline{T}_a$ is $\overline{R}_a$. Therefore, the output voltage is a linear function of the ambient temperature and its sensitivity to ambient temperature change is

$$\left.\frac{\partial \overline{V}}{\partial \overline{T}_a}\right|_{CC} = \alpha_R \bar{I} R_0 (1 + a_{R0}) = \alpha_R \overline{V}_0 \tag{3.40}$$

where

$$a_{R0} = \frac{\overline{R} - R_0}{R_0} = \alpha_R (\overline{T}_a - T_0) \tag{3.41}$$

is the sensor resistance over-heat ratio at room temperature T_0. The measured sensitivities labeled in Figure 3.10 are in good agreement with those calculated from Eq. (3.40).

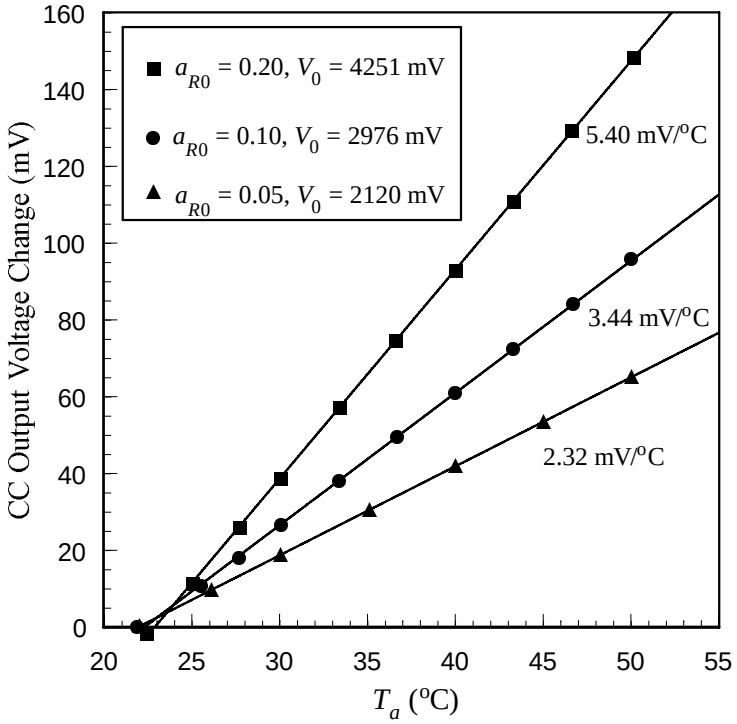

Figure 3.10 Output voltage sensitivity of the sensor to ambient temperature in CC mode.

The conventional constant temperature (CT) anemometer circuit shown in Figure 2.13 with temperature insensitive bridge resistors keeps the sensor resistance and hence the sensor temperature constant. In CT mode, both $\bar{I}$ and $\overline{R}_a$ change with $\overline{T}_a$. The theoretical $\overline{V} - \overline{T}_a$ curves calculated from Eq. (3.38) (Figure 3.11) exhibit severe non-linearity when the ambient temperature becomes close to the sensor temperature. For

small fluctuation of ambient temperature around room temperature, the temperature sensitivity can be expressed as

$$\left.\frac{\partial \overline{V}}{\partial \overline{T}_a}\right|_{CT} \approx -\left(1+\frac{1}{a_R}\right)\frac{\alpha_R V_0}{2} \tag{3.42}$$

which means that the temperature sensitivity is higher when the sensor is operated at smaller over-heat ratio. The sensitivities extracted from the experimental results shown in Figure 3.11 are close to those calculated from the above equation (-14.0 mV/^{o}C, -17.9 mV/^{o}C and -24.7 mV/^{o}C for a_R = 0.2, 0.1 and 0.05 respectively). However, the results for small over-heat ratios deviate significantly from the theoretical curves. As a matter of fact, the measured $\overline{V} - \overline{T}_a$ relationships are more linear than expected.

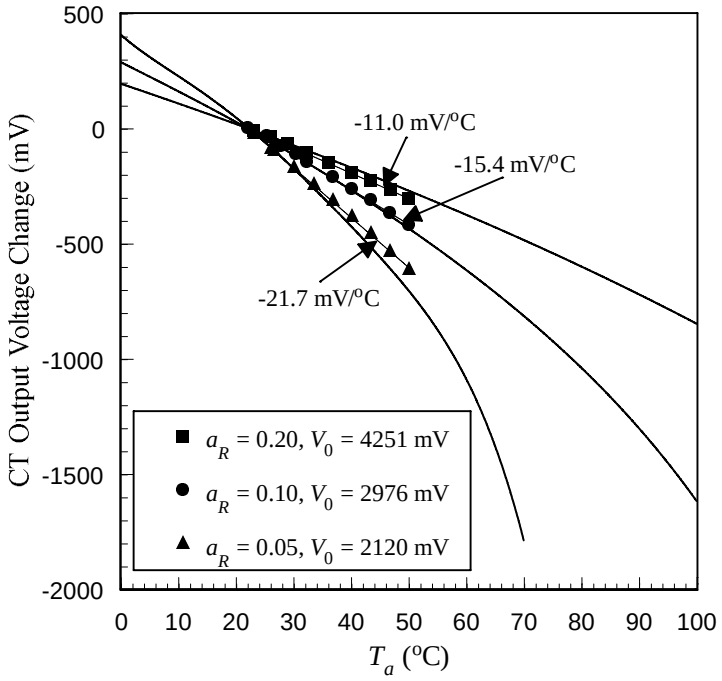

Figure 3.11 Ambient temperature sensitivity of the sensor output voltage in CT mode. The sensor temperatures corresponding to the over-heat ratios of 0.05, 0.10 and 0.20 are 73^{o}C, 123 ^{o}C and 223 ^{o}C respectively.

In an ideal CT mode, the sensor temperature is preset to a value by the three temperature-insensitive bridge resistors. Obviously, the sensor will not function when the ambient temperature becomes equal to the preset sensor temperature. Therefore, in most

applications, the sensor is operated at a temperature significantly higher than the room temperature to avoid the situation. This has the additional advantage of reducing and linearizing (for easy compensation) the output drift with ambient temperature. However, in some applications, such as in underwater measurement, high operating temperature is undesirable. This problem can be solved by integrating the bridge resistor R_3 (or all of the resistors) with the sensor on the same chip. Because the bridge resistors are in direct contact with the substrate, they will not be heated up by electrical current. However, their resistance will change with ambient temperature since the resistors and the sensor are made of the same material and they all have the same temperature coefficient of resistance. As a result, we have

$$\overline{T}_s - \overline{T}_a = [1 + \alpha_R(\overline{T}_a - T_0)]\frac{a_{R0}}{\alpha_R} = \frac{\overline{R}_a}{R_0}\frac{a_{R0}}{\alpha_R} \tag{3.43}$$

i.e., the temperature difference between the sensor and the ambient is proportional to $\overline{R}_a$. According to Eq. (3.21), $\bar{I}$ is not a function of $\overline{T}_a$ and the temperature sensitivity then is

$$\frac{\partial \overline{V}}{\partial \overline{T}_a} = \alpha_R \bar{I} R_0 \frac{\partial \overline{T}_s}{\partial \overline{T}_a} = \alpha_R \overline{V}_0 \tag{3.44}$$

which is the same as that in CC mode. Note that the sensor temperature does not change with the heat transfer coefficient. Therefore, the sensitivity to heat transfer is the same as that in CT mode.

In conclusion, this type of simple compensation results in a new mode having the advantages of both CC mode (low temperature sensitivity) and CT mode (high sensitivity to heat transfer coefficient, as will be demonstrated in the next section) at any operation temperature.

3.4.3 Sensitivity to Shear Stress

The output sensitivity to heat transfer in CC mode

$$\left.\frac{\partial \bar{V}}{\partial \bar{h}}\right|_{CC} = -\frac{\alpha_R \bar{I}^3 R_0 \bar{R}_a}{{\lambda_0}^4 (\kappa d)_e{}^2 wl}\left[1-\frac{3}{\lambda_0 l}\tanh\left(\frac{\lambda_0 l}{2}\right)+\frac{1}{2\cosh^2(\lambda_0 l/2)}\right] \left[1+\frac{2d+2d_2}{w}+\frac{1/(\delta_0 w)}{\tanh(\delta_0 L')}-\frac{L'/w}{\sinh^2(\delta_0 L')}\right] \tag{3.45}$$

and the sensitivity to heat transfer in CT mode

$$\left.\frac{\partial \bar{V}}{\partial \bar{h}}\right|_{CT} = \frac{\dfrac{\bar{V}}{2\lambda^2(\kappa d)_e}\left[1+\dfrac{2d+2d_2}{w}+\dfrac{1/(\delta w)}{\tanh(\delta L')}-\dfrac{L'/w}{\sinh^2(\delta L')}\right]}{\left[1-\dfrac{2}{\lambda l}\tanh(\dfrac{\lambda l}{2})\right]\Big/\left[1-\dfrac{3}{\lambda l}\tanh(\dfrac{\lambda l}{2})+\dfrac{1}{2\cosh^2(\dfrac{\lambda l}{2})}\right]+\dfrac{\alpha_R \bar{I}^2 R_0}{\lambda^2 (\kappa d)_e wl}} \tag{3.46}$$

are still functions of the heat transfer coefficient, as shown in Figure 3.12. However, in a sufficiently small range, the output voltage changes are proportional to the change of heat transfer coefficient in small range (Figure 3.13).

The relationship between the heat transfer coefficient h and the wall shear stress τ_w when the sensor is flush-mounted on the wall has been experimentally determined or theoretically derived by a number of researchers [8,9,11,19]. The most general expression is the one reported by Brown, who included the effect of pressure gradient, that is,

$$Nu^3 = A\tau_w + \frac{B}{Nu}\frac{dp}{dx}L \tag{3.47}$$

where A and B are constants, *Nu* is the *Nusselt* number, which is defined as $h_c l/\nu$ with l being the characteristic length, L the effective length of the sensor in the streamwise direction, and $h_c = \Delta h$ the heat transfer coefficient caused by forced convection. If the pressure drop across the sensor is small, which is usually the case for our micro sensors in subsonic flow, the second term in the above equation can be neglected. Then we have

$$h_c = \Delta h \propto {\tau_w}^{1/3} \tag{3.48}$$

The measured output voltage changes in CC and CT modes with wall shear stress are plotted in Figure 3.14 and Figure 3.15 respectively. The solid lines in the figures are

polynomial fittings. By comparing these measured data with the calculated data (Figure 3.12), we found that the maximum variation of the heat transfer coefficient in our calibration is less than 0.016 W/cm^{2}.^{o}C or about 6%, well in the linear region of the $\Delta\overline{V} - \Delta\overline{h}$ curves in Figure 3.13. Theoretically, if we plot the voltage change against $\tau_w^{1/3}$, we should be able to get straight lines, except in the very low shear stress region, where measurement errors and non-idealities occur. However, in reality, when the shear stress range is less than 1 Pa, it is difficult to determine the exponent to the shear stress because the accuracy of fitting is not very sensitive to it.

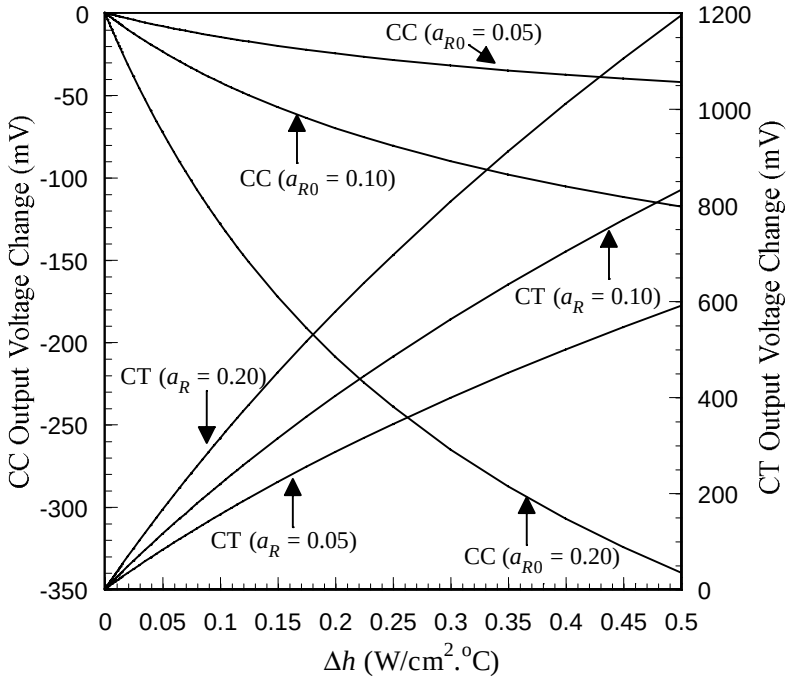

Figure 3.12 Output voltage changes as a function of heat transfer coefficient at different over-heat ratios for the 3.3 μm wide sensor.

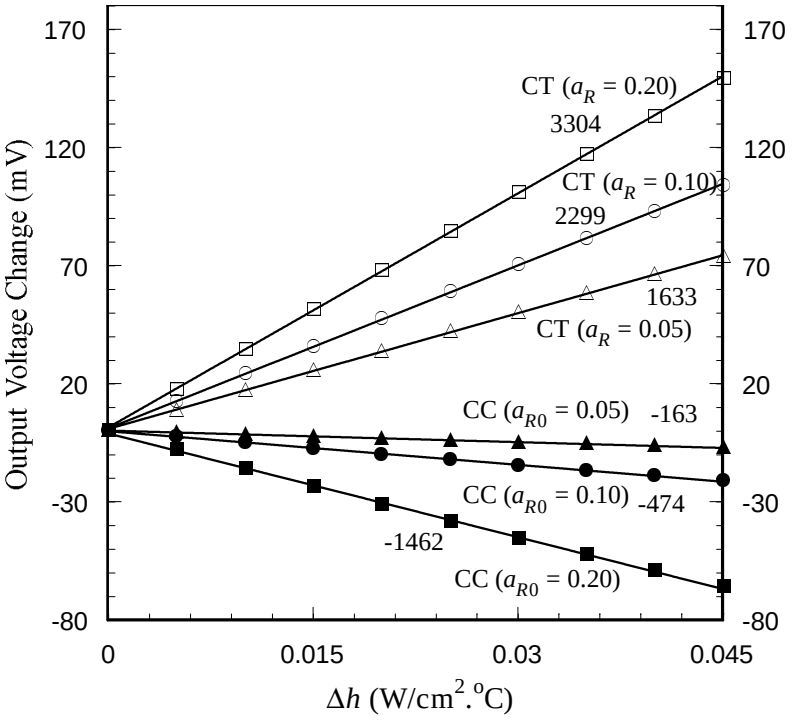

Figure 3.13 Zoom-in of the calculated $\overline{V}$ – $\Delta\overline{h}$ curves in the linear region.

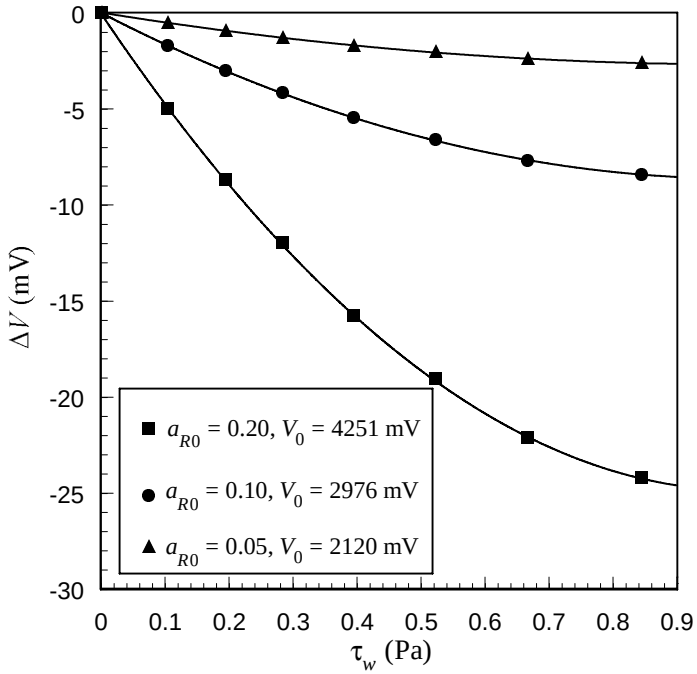

Figure 3.14 Output voltage changes in CC mode at different over-heat ratios. The normalized output ($\Delta V/V_0$) increases dramatically with over-heat ratio.

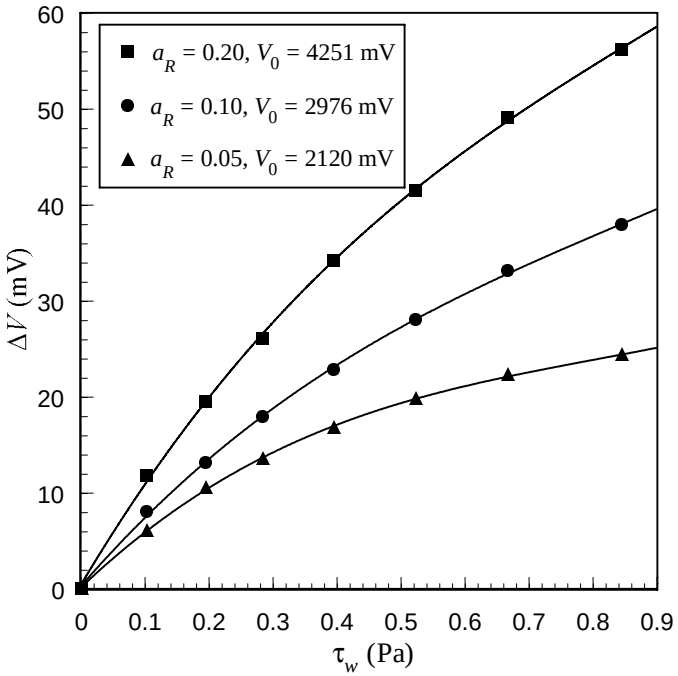

Figure 3.15 Output voltage changes in CT mode at different over-heat ratios. The normalized output is almost insensitive to the over-heat ratio.

Both the theoretical calculations and experimental data have shown that the normalized output in CC mode increases dramatically for larger over-heat ratio, which implies high over-heat ratio for CC operation in order to get enough sensitivity. For CT operation, the normalized output is almost insensitive to the over-heat ratio in CT mode. However, reasonably high over-heat ratio is still preferred to avoid excessive temperature sensitivity.

The drift of the sensitivity to heat transfer with ambient temperature can be estimated from Eqs. (3.45) and (3.46). In CC mode, this drift is linearly proportional to the ambient temperature change with the coefficient of proportionality being $\alpha_R \approx 0.1\%/^{o}C$. In CT mode, the sensitivity - ambient temperature relationship has been numerically calculated and is plotted in Figure 3.16. The drift rates around room temperature are labeled next to each curve. In all cases, the drift rate is no more than $1\%/^{o}C$ and can be neglected when the sensors are used in laboratory measurement where ambient temperature change is

only a few degrees. For applications where ambient temperatures varies significantly, temperature compensation to the output voltage is necessary. This may be complicated at small over-heat ratio in CT mode due to the high non-linearity. If the integrated bridge temperature compensation scheme described in the previous section can be used, the drift of sensitivity with ambient temperature in CT mode becomes that in CC mode and can be further reduced by linear compensation.

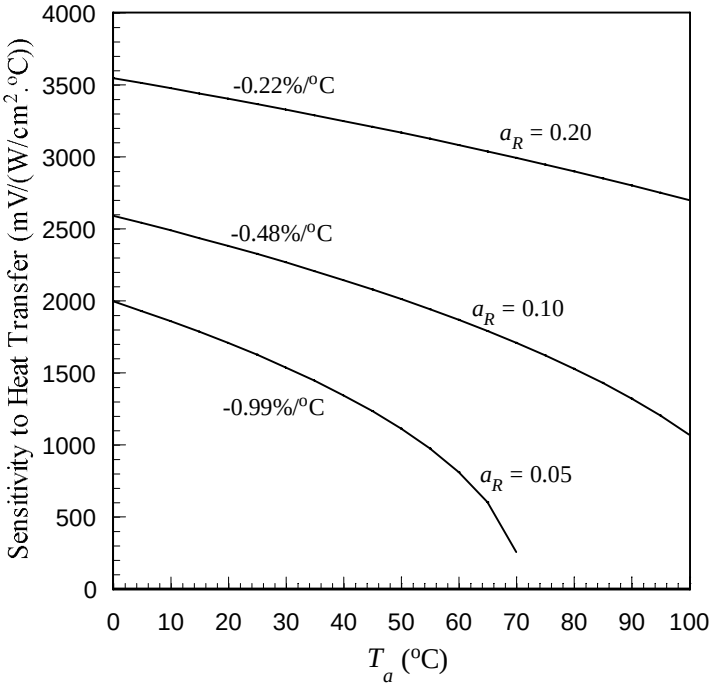

Figure 3.16 The drift of the sensitivity to heat transfer coefficient with ambient temperature in CT mode.

Finally, Figure 3.17 shows that wind-tunnel calibration results of the sensors with different widths. This time, we have plotted the normalized voltage changes against $\tau_w^{1/3}$. Again, the normalized sensitivity is almost independent of the sensor width.

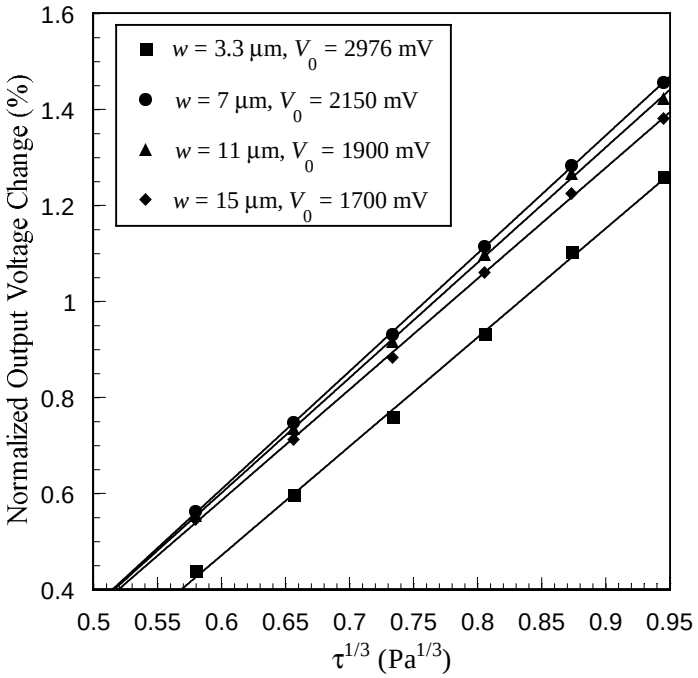

Figure 3.17 Wind-tunnel calibration results of the sensors with different width at the over-heat ratio of 0.1.

3.4.4 Frequency Responses in CC Mode

The frequency response of r_b(s) is the only one among the three ac components in the equivalent circuit of the sensor that can be experimentally measured since standard perturbation on heat transfer or wall shear stress and ambient temperature are not readily available. The simple circuit shown in Figure 3.18 has been used to do the measurement. The function generator supplies both the dc bias and the ac sine wave signal to the Wheatstone bridge through a wide-band voltage follower. The values of R_1, R_2 and R_3 are chosen such that $R_1 R_3 = R_2 R_0 (1 + a_R)$, where a_R is the desired over-heat ratio of the sensor. The dc output of the bridge can be nulled by adjusting the dc bias. At that point, we know that the sensor has been biased at the right over-heat ratio. The amplitude of the sine wave is set to about 3% of the dc bias to satisfy the small signal condition. The frequency of the sine wave is swept from 2 Hz to 100 kHz while the magnitude and phase of the amplified output are recorded. The magnitude and phase of $r_b(i\omega)$ can thus be calculated from these measurement results by

$$\left|r_b(i\omega)\right| = \frac{\left(1+\frac{R_3}{R_2}\right)R_1}{\left\{\left[\frac{R_2}{R_2+R_3}\left|\frac{Gv_i(i\omega)}{v_o(i\omega)}\right|\right]^2 - \frac{2R_2\cos\theta}{R_2+R_3}\left|\frac{Gv_i(i\omega)}{v_o(i\omega)}\right| + 1\right\}^{\frac{1}{2}}} \tag{3.49}$$

$$\phi = -\tan^{-1}\frac{\sin\theta}{\cos\theta - \frac{R_2+R_3}{R_2}\left|\frac{v_o(i\omega)}{Gv_i(i\omega)}\right|} \tag{3.50}$$

where v_i is the input signal from the function generator, v_o is the amplified output signal, G is the gain of the amplifier after the Wheatstone bridge and θ is the phase of the output signal.

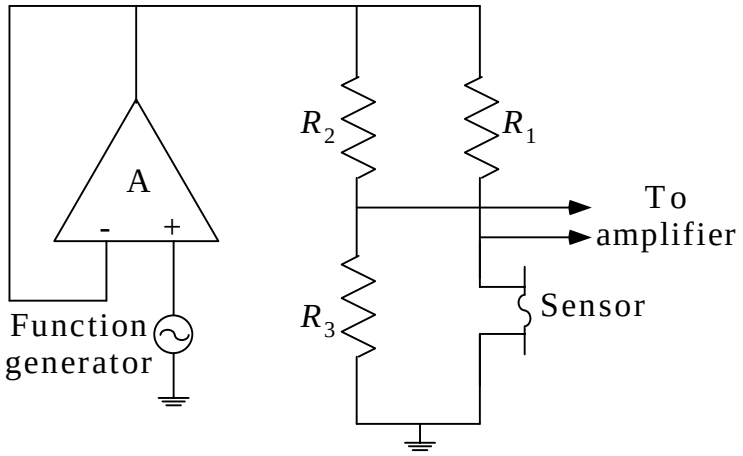

Figure 3.18 Circuit used in measuring the frequency response of the sensors in CC mode.

The Bode plots of the magnitude and phase responses for the sensors with different widths are shown in Figure 3.19 and Figure 3.20 respectively. The solid lines are the fitted curves of Eq. (3.35) using the parameters in Tables 3.1 and 3.2. Note that the fitting parameters f_1 and f_2 are in reasonably good agreement with their calculated values.

Table 3.2 Calculated and fitted parameters for the study of dynamic responses.

w (μm)	b	f_1 (Hz)		f_2 (Hz)	
	Calculated	Calculated	Fitted	Calculated	Fitted
3.3	1.173	140	133	2322	3400
7	1.193	140	135	1076	1150
11	1.130	140	130	723	690
15	1.081	140	126	554	480

Unlike the conventional hot-wire anemometers and flush-mountable hot-film sensors, which have constant high frequency roll-off of 20 dB/dec. [20,21] and 10 dB/dec. [22] respectively, the micromachined shear stress sensors do not exhibit a constant roll-off at high frequency. Their frequency responses are the result of the coupling of two critical frequencies, f_1 and f_2. f_1 represents the thermal response of the diaphragm and is virtually independent of the sensor width; f_2 represents the thermal response of the sensing element and decreases with increasing sensor width. As a matter of fact, this model can be used to qualitatively explain the behavior of hot-wire and hot-film sensors. For a free-standing hot wire (i.e., no substrate), f_1 is infinity and according to Eqs. (3.35) and (3.28), the maximum attenuation rate of the magnitude-frequency response is inversely proportional to the frequency with f_2 being the corner frequency. For a hot-film sensor (thin metal sensing element directly sitting on thick and flat substrate, such as quartz), f_1 is typically a few Hz, while f_2 is usually in the kilo-Hertz range. Therefore the maximum attenuation rate of the magnitude-frequency response is inversely proportional to the square root of frequency in the region between 10 Hz to 1 kHz.

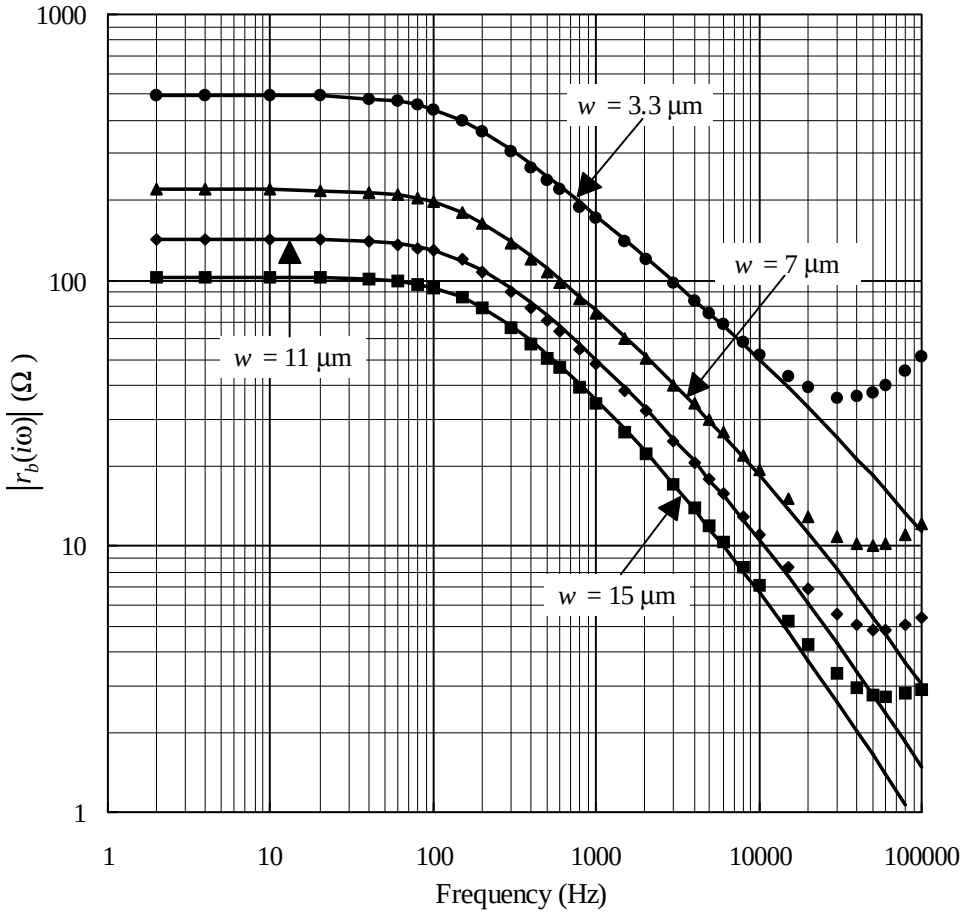

Figure 3.19 Magnitude responses of $r_b(i\omega)$ for sensors with different widths.

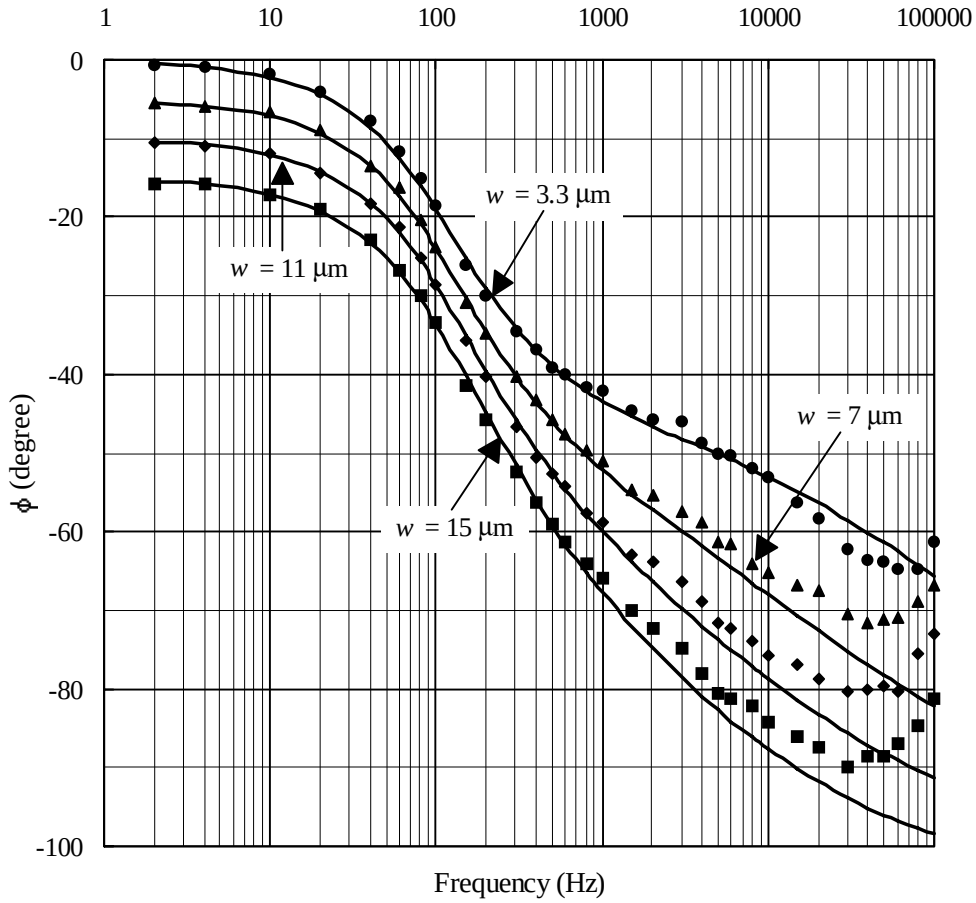

Figure 3.20 Phase responses of $r_b(i\omega)$ for sensors with different widths. Note that the curves for 7 μm, 11 μm and 15 μm have been shifted down by 5, 10 and 15 degrees respectively to avoid overlapping with other curves.

As can be seen from the figures, the experimental data points start to deviate from the theoretical curves at frequency of 10 kHz. It is even more surprising that, above certain frequency (40 kHz, 60 kHz, 80 kHz and 80 kHz for w = 3.3 μm, 7 μm, 11 μm and 15 μm respectively), the magnitude of r_b increases with frequency. This abnormal effect is obviously caused by the parasitic components from the sensing element in the measurement circuit.

Finally, the voltage sensitivity $G_h(i\omega)$ and $G_T(i\omega)$ are plotted against the excitation frequencies. They both have a corner frequency at about 130 Hz. It is interesting that these two sensitivities attenuate at frequencies above f_1 with a constant rate of 20 dB/dec.,

even for all the sensors under study. This can be qualitatively explained by the simple heat transfer model of the sensor structure. Since the size of the sensing element is small, most of its generated heat is lost to the diaphragm, which in turn loses heat to the ambient. These two heat transfer steps each has an attenuation rate proportional to the square root of frequency. The overall attenuation is then proportional to the frequency.

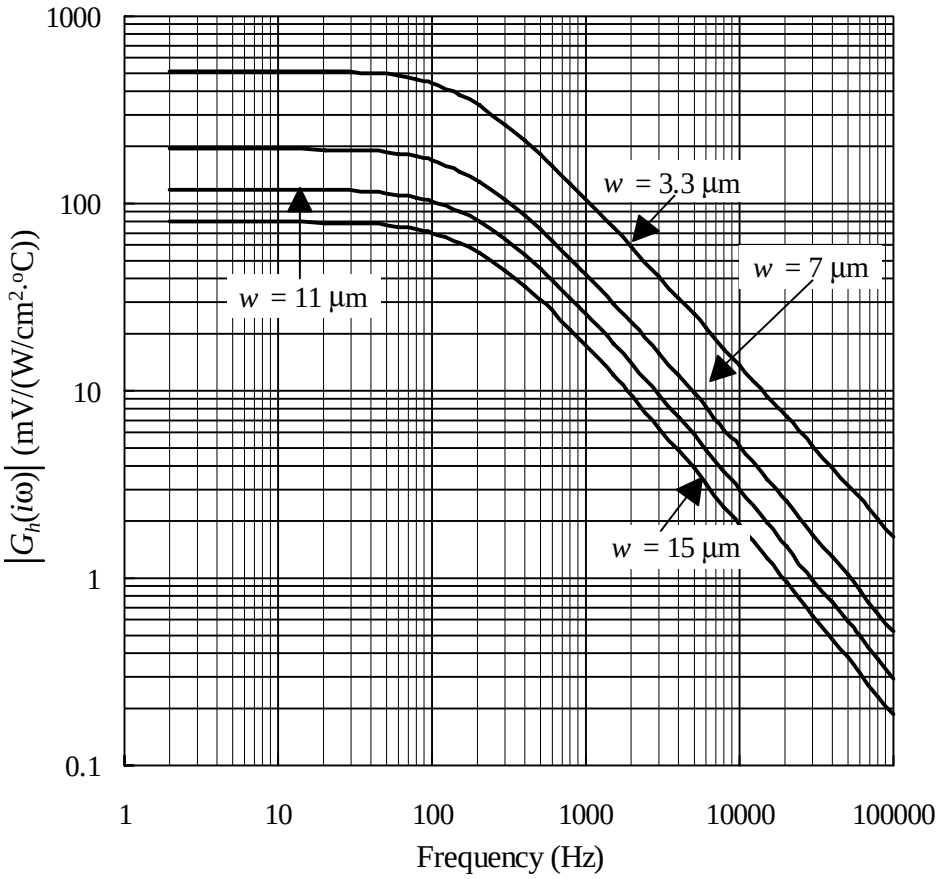

Figure 3.21 Magnitude responses of $G_h(i\omega)$.

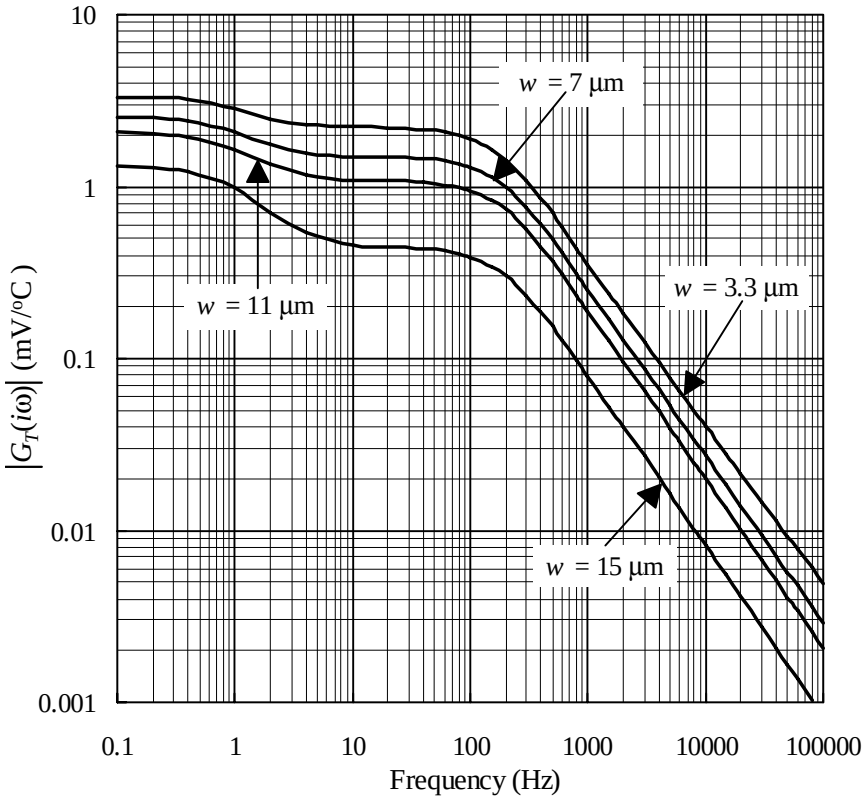

Figure 3.22 Magnitude responses of $G_T(i\omega)$.

In addition to the corner frequency at 130 Hz, $G_T(i\omega)$ has another much lower corner frequency at 1 Hz (assumed), as a result of the slow response of the silicon substrate to ambient temperature change. The ac temperature sensitivity on the second platform in the Bode plot is only 50% - 70% of that at steady state. This difference, if not corrected, could cause significant error in the measurement of temperature fluctuation.

3.4.5 Frequency Responses in CT Mode

Figure 2.13 is the schematic of the constant temperature bias circuit. It is easy to derive from the equivalent circuit of the sensor (Figure 3.5) and the basic circuit theory that the voltage at the non-inverting input terminal of the operational amplifier is

$$v_+ = R_2' \| R_3' \left(\frac{v_o}{R_2} + \frac{v_t}{R_t} \right) \tag{3.51}$$

where $R_2' = R_2 \| R_t = \frac{R_2 R_t}{R_2 + R_t}$ and $R_3' = R_3 \| R_r = \frac{R_3 R_r}{R_3 + R_r}$, and the voltage at the inverting input terminal of the operational amplifier is

$$v_- = \frac{[\overline{R} + r_b(s)]v_o + R_1[G_h(s)\tilde{h} + G_T(s)\tilde{T}_a]}{R_1 + \overline{R} + r_b(s)} \tag{3.52}$$

Considering the great complexity of the expression for $r_b(s)$ (Eq. (3.35)), we will continue to use the symbol $r_b(s)$ and its polar expression $r_b(s) = |r_b|e^{i\phi}$ throughout the remaining derivation just for simplicity. The equation for an operational amplifier with two poles is

$$v_o = \frac{A_0 v_i}{(1 + \frac{s}{p_1})(1 + \frac{s}{p_2})} = \frac{A_0(v_+ - v_-)}{1 + sM' + s^2 M''} \tag{3.53}$$

where p_1 and p_2 are the first and second pole frequencies, $M' = \frac{1}{p_1} + \frac{1}{p_2}$ and $M'' = \frac{1}{p_1 p_2}$. Inserting Eqs. (3.51) and (3.52) into the above equation yields

$$\frac{1 + sM' + s^2 M''}{A_0} v_o = R_2' \| R_3' \left(\frac{v_o}{R_2} + \frac{v_t}{R_t} \right) - \frac{[\overline{R} + r_b(s)]v_o + R_1[G_h(s)\tilde{h} + G_T(s)\tilde{T}_a]}{R_1 + \overline{R} + r_b(s)} \tag{3.54}$$

$$\begin{aligned} v_o &= \frac{\frac{R_2' \| R_3'}{R_t} v_t - \frac{R_1[G_h(s)\tilde{h} + G_T(s)\tilde{T}_a]}{R_1 + \overline{R} + r_b(s)}}{\frac{1 + sM' + s^2 M''}{A_0} - \frac{R_2' \| R_3'}{R_2} + \frac{\overline{R} + r_b(s)}{R_1 + \overline{R} + r_b(s)}} \\ &= \frac{\frac{R_2' \| R_3'}{R_t}\left[\frac{R_1 + \overline{R}}{r_b(s)} + 1\right] v_t - \frac{R_1}{r_b(s)}[G_h(s)\tilde{h} + G_T(s)\tilde{T}_a]}{\left(\frac{1 + sM' + s^2 M''}{A_0} - \frac{R_2' \| R_3'}{R_2}\right)\left[\frac{R_1 + \overline{R}}{r_b(s)} + 1\right] + \frac{\overline{R}}{r_b(s)} + 1} \end{aligned} \tag{3.55}$$

Since the bridge is balanced in steady state, it is easy to show that

$$\frac{\overline{R}}{R_1} = \left[1 - \frac{R_2^{'} \| R_3^{'}}{R_2}\left(1 + \frac{R_2}{R_r}\frac{V_r}{V_o}\right)\right]^{-1} - 1 \tag{3.56}$$

For convenience, the resistors in the CT circuit are chosen such that $R_2 = R_3 << R_t = R_r$. Then,

$$\frac{\overline{R}}{R_1} = 1 + \frac{2R_2}{R_r}\left(\frac{V_r}{V_o} - 1\right) \tag{3.57}$$

$$\begin{aligned} v_o &= \frac{\frac{R_2}{2R_t}\left(\frac{2R_1}{|r_b|}e^{-i\phi} + 1\right)v_t - \frac{R_1}{r_b(s)}[G_h(s)\tilde{h} + G_T(s)\tilde{T}_a]}{\frac{sM^{'} + s^2M^{''}}{A_0}\left(\frac{2R_1}{|r_b|}e^{-i\phi} + 1\right) + \frac{R_2}{R_r}\left(1 + \frac{R_1}{|r_b|}\frac{V_r}{V_o}e^{-i\phi}\right) + \frac{1}{2}} \\ &= \frac{\frac{R_2}{R_t}\left[\left(1 + \frac{2R_1}{|r_b|}\cos\phi\right) - i\left(\frac{2R_1}{|r_b|}\sin\phi\right)\right]v_t - \frac{2R_1}{r_b(s)}[G_h(s)\tilde{h} + G_T(s)\tilde{T}_a]}{p(\omega) + iq(\omega)} \end{aligned} \tag{3.58}$$

where

$$p(\omega) = 1 + \frac{4\omega M^{'}}{A_0}\frac{R_1}{|r_b|}\sin\phi - \frac{2\omega^2 M^{''}}{A_0}\left(1 + \frac{2R_1}{|r_b|}\cos\phi\right) + \frac{R_2}{R_r}\left(1 + \frac{2R_1}{|r_b|}\frac{V_r}{V_o}\cos\phi\right) \tag{3.59}$$

and

$$q(\omega) = \frac{2\omega M^{'}}{A_0}\left(1 + \frac{2R_1}{|r_b|}\cos\phi\right) + \frac{4\omega^2 M^{''}}{A_0}\frac{R_1}{|r_b|}\sin\phi - \frac{2R_1}{|r_b|}\frac{R_2}{R_r}\frac{V_r}{V_o}\sin\phi \tag{3.60}$$

The magnitude of the gain is

$$\left|\frac{v_o}{v_t}\right| = \frac{R_2}{R_t}\frac{\left[\left(1 + \frac{2R_1}{|r_b|}\cos\phi\right)^2 + \left(\frac{2R_1}{|r_b|}\sin\phi\right)^2\right]^{\frac{1}{2}}}{\left[p(\omega)^2 + q(\omega)^2\right]^{\frac{1}{2}}} \tag{3.61}$$

The phase angle of the gain is

$$\varphi = -\tan^{-1}\frac{\sin\phi}{\cos\phi + \dfrac{|r_b|}{2R_1}} - \tan^{-1}\frac{q(\omega)}{p(\omega)} \tag{3.62}$$

The sensitivity to heat transfer coefficient is

$$\left|\frac{v_o}{\tilde{h}}\right| = \frac{2R_1\left|\dfrac{G_h(s)}{r_b(s)}\right|}{\left[p(\omega)^2 + q(\omega)^2\right]^{\frac{1}{2}}} = \frac{2R_1\left|\dfrac{G_h(s)}{r_b(s)}\right|\left|\dfrac{v_o}{v_t}\right|\dfrac{R_t}{R_2}}{\left[\left(1+\dfrac{2R_1}{|r_b|}\cos\phi\right)^2 + \left(\dfrac{2R_1}{|r_b|}\sin\phi\right)^2\right]^{\frac{1}{2}}} \tag{3.63}$$

The sensitivity to ambient temperature fluctuation is

$$\left|\frac{v_o}{\overline{T}_a}\right| = \frac{2R_1\left|\dfrac{G_h(s)}{r_b(s)}\right|}{\left[p(\omega)^2 + q(\omega)^2\right]^{\frac{1}{2}}} = \frac{2R_1\left|\dfrac{G_T(s)}{r_b(s)}\right|\left|\dfrac{v_o}{v_t}\right|\dfrac{R_t}{R_2}}{\left[\left(1+\dfrac{2R_1}{|r_b|}\cos\phi\right)^2 + \left(\dfrac{2R_1}{|r_b|}\sin\phi\right)^2\right]^{\frac{1}{2}}} \tag{3.64}$$

If the op-amp has only one pole, i.e., $M'' = 0$,

$$p(\omega) = 1 + \frac{4\omega M'}{A_0}\frac{R_1}{|r_b|}\sin\phi + \frac{R_2}{R_r}\left(1 + \frac{2R_1}{|r_b|}\frac{V_r}{V_o}\cos\phi\right) \tag{3.65}$$

$$q(\omega) = \frac{2\omega M'}{A_0}\left(1 + \frac{2R_1}{|r_b|}\cos\phi\right) - \frac{2R_1}{|r_b|}\frac{R_2}{R_r}\frac{V_r}{V_o}\sin\phi \tag{3.66}$$

In most of our experimental studies on the sensor frequency responses in CT mode, OP-27 has been used as the feedback amplifier. It has a single pole and is unity gain stable. Its gain-bandwidth product is about 7 MHz. In the measurement of the gain, the amplitude of the sine wave testing signal v_t is adjusted to ensure that the output signal satisfies the small signal criteria, i.e., $v_o << V_o$. R_2 and R_3 are both 5 kΩ, R_t and R_r are 1 MΩ, a_r = 0.1, V_r = 4.2 V for all types of sensors when the circuit is in critical damping

state. The measured magnitude and phase responses of the gain to frequency are then shown in Figure 3.23 and Figure 3.24. The solid lines are the theoretical curves calculated from Eqs. (3.61) and (3.62) with $|r_b|$ and ϕ being the fitted data obtained in Section 3.4.3.

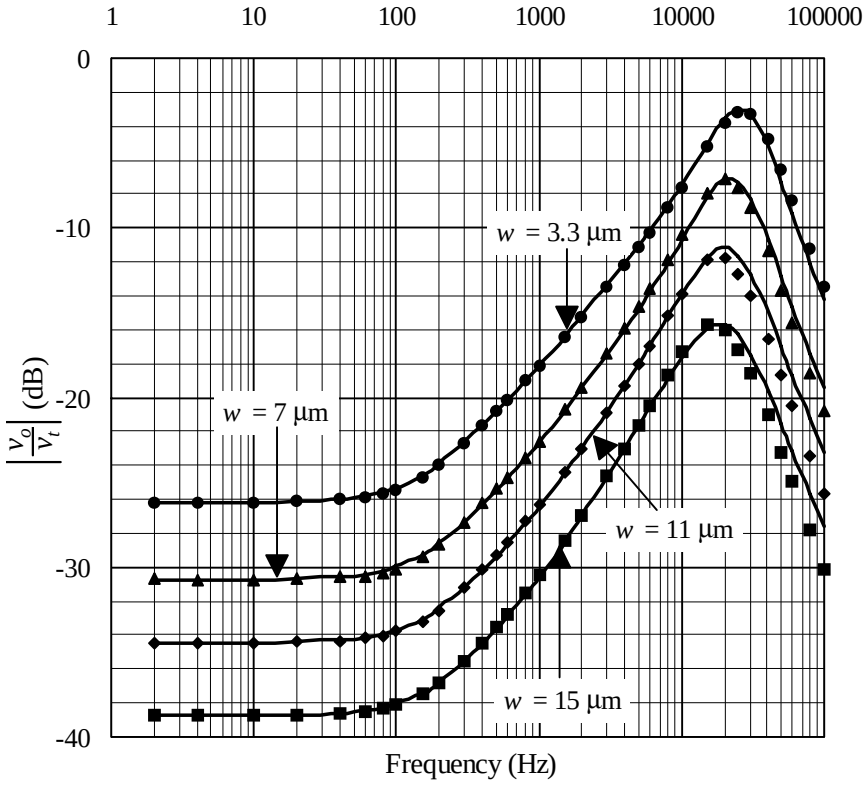

Figure 3.23 Magnitude responses of the gain of the CT circuit at a_R = 0.1.

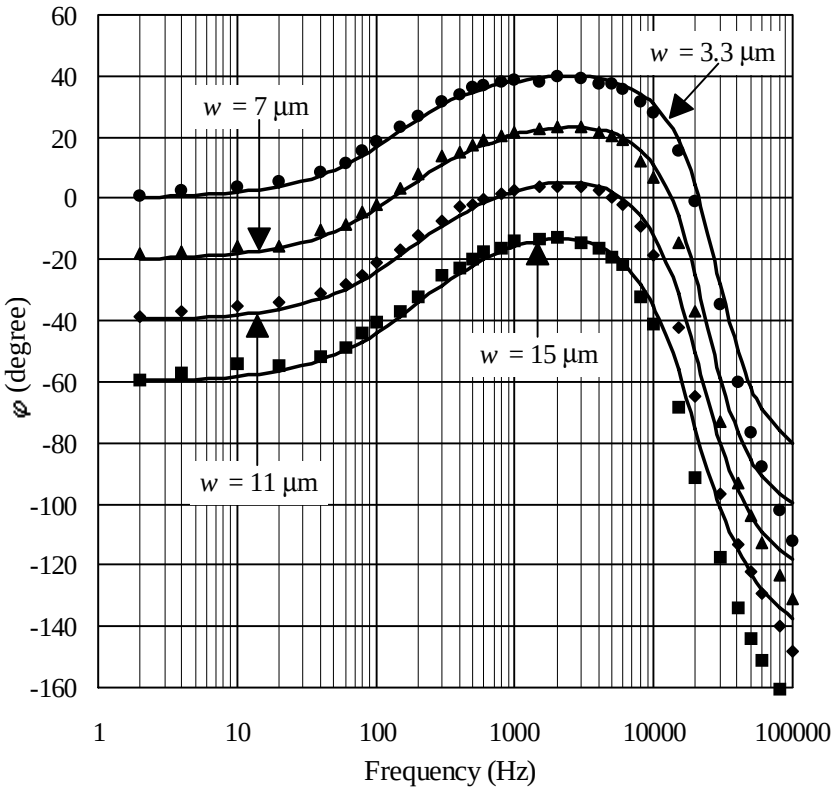

Figure 3.24 Phase responses of the gain of the CT circuit.

The magnitude of the gain is almost inversely proportional to $|r_b(i\omega)|$ before reaching the peak. The frequency at the peak is the critical frequency of the system to electronic signals. It has also been assumed to be the cut-off frequency of the system to flow signals. According to Eq. (3.63), this assumption is correct for conventional hot-wire and some hot-film sensors where $r_b(i\omega)$and $G_h(i\omega)$ have the same frequency responses. However, in the previous section, they have been found to have significantly different frequency responses for our sensors. We can therefore expect a somewhat non-flat magnitude response of our CT sensor systems to flow signals even below the critical frequency (Figure 3.25 and Figure 3.26) and certain compensation in data processing such as using FFT is necessary for some applications.

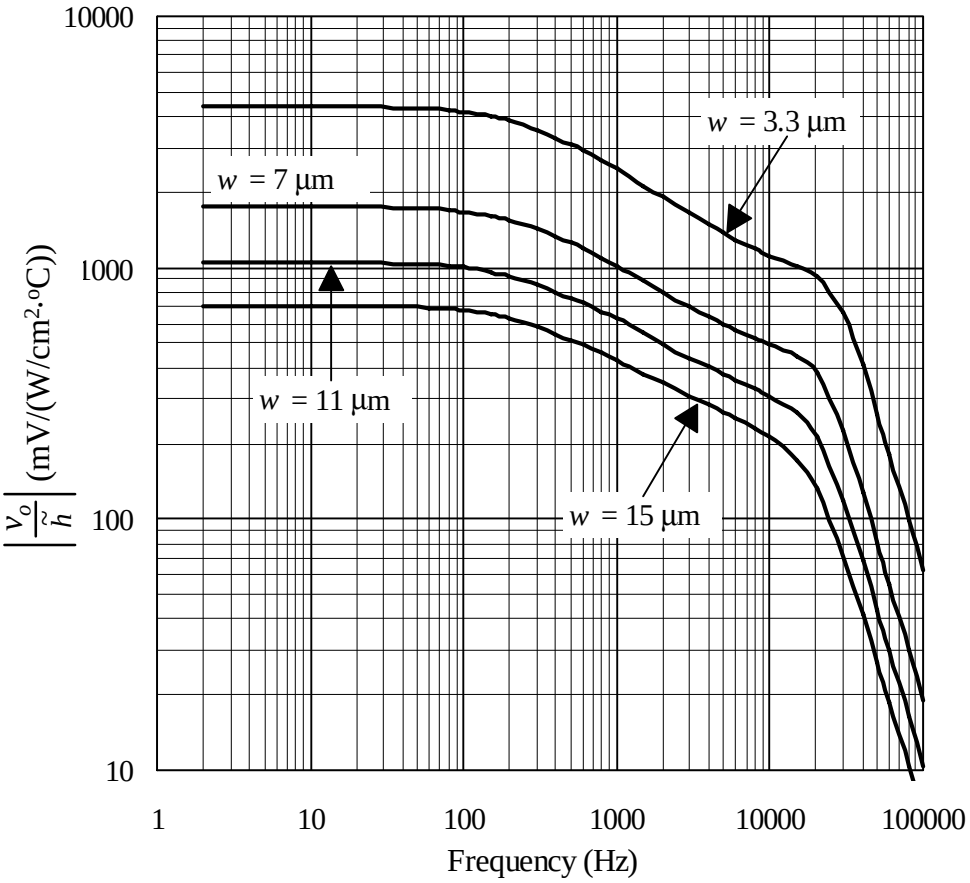

Figure 3.25 Calculated frequency response of the sensitivity to heat transfer coefficient in CT mode.

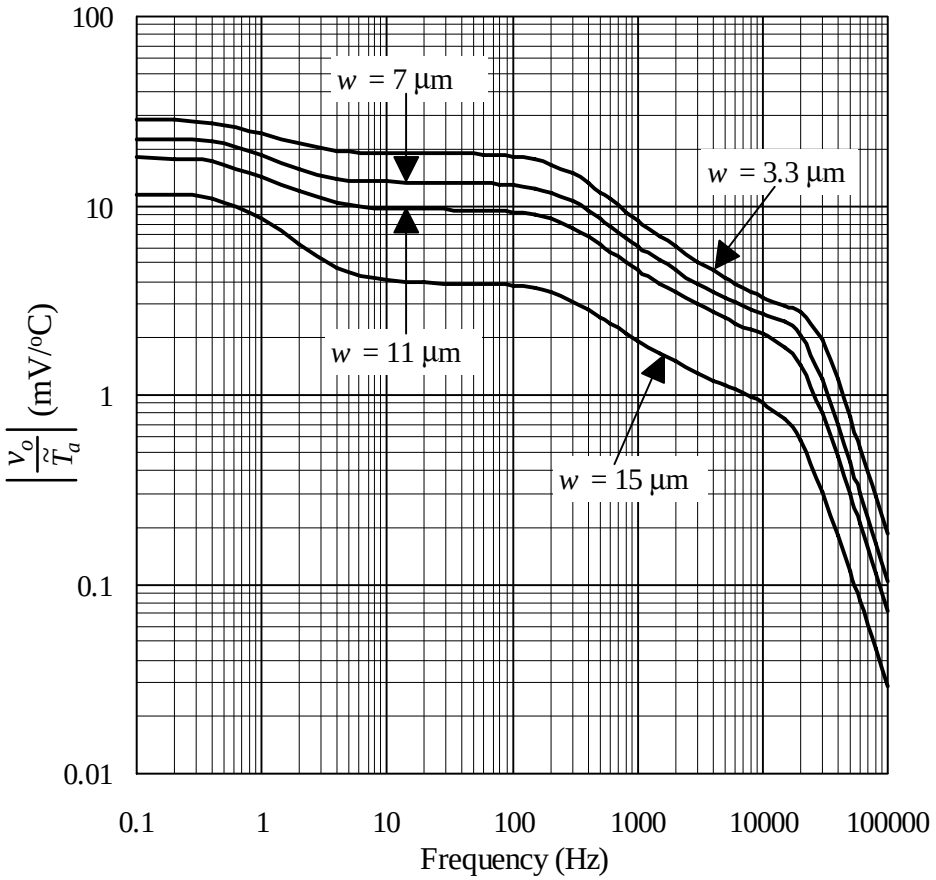

Figure 3.26 Calculated frequency response of the temperature sensitivity in CT mode.

The critical frequency of the CT circuit can be boosted by using improved circuits and op-amps with higher gain-bandwidth products. We will not discuss it here because it is beyond the scope of our research. The non-flat frequency response of the sensitivity to heat transfer below the critical frequency can be improved by optimizing the design of the sensor, including the increase on the horizontal dimensions (especially the width) of the polysilicon resistor while to equalize the frequency responses of $r_b(i\omega)$ and $G_h(i\omega)$. The underlying principle of the improvement, of course, is the reduction of the conduction heat loss from the polysilicon resistor to the nitride diaphragm through the sides and through the ends.

3.5 Comparison with Conventional Hot-Film Sensors

Table 3.3 Comparison of conventional and micromachined shear stress sensors.

Parameters	Conventional	Micromachined
Sensor dimension	mm size	250×250 μm2
Resistance	10 - 100 Ω	400 - 2.5 kΩ
Sensitivity (mV/Pa)	< 10	> 50
Frequency bandwidth (CC)	< 10 Hz	> 100 Hz
Power consumption (mW)	> 40	5

3.6 Other Structures

In addition to the vacuum-isolated shear stress sensor (type I) described above, we have also fabricated and studied other possible structures that can be used as shear stress sensors [23]. Their cross-sections and SEM pictures are shown in Figure 3.27. Type II has a similar structure to type I except that the polysilicon wire is lifted a few microns above the diaphragm, thus achieving better thermal isolation. Type III is a conventional polysilicon bridge sitting on the solid substrate [24,25]. Type IV is basically a micromachined hot wire which is very close to the wall. All these wires are a few microns (in a range from 1 μm to 5 μm) above the substrate surface so they are well in viscous sublayer, i.e., the linear velocity distribution region and the heat transfer is still a function of wall shear stress [11]. In our study, all four types of structures were fabricated on a single chip to ensure identical thermal and electrical properties of the sensing elements.

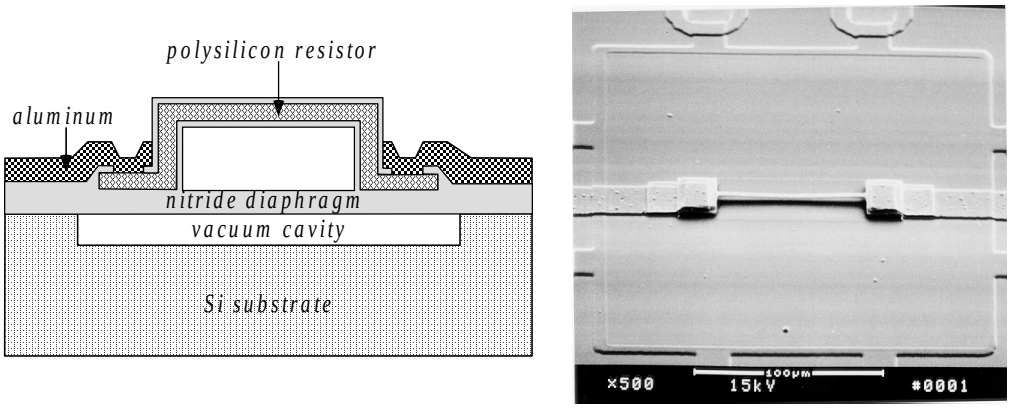

(a) Type II: bridge over diaphragm.

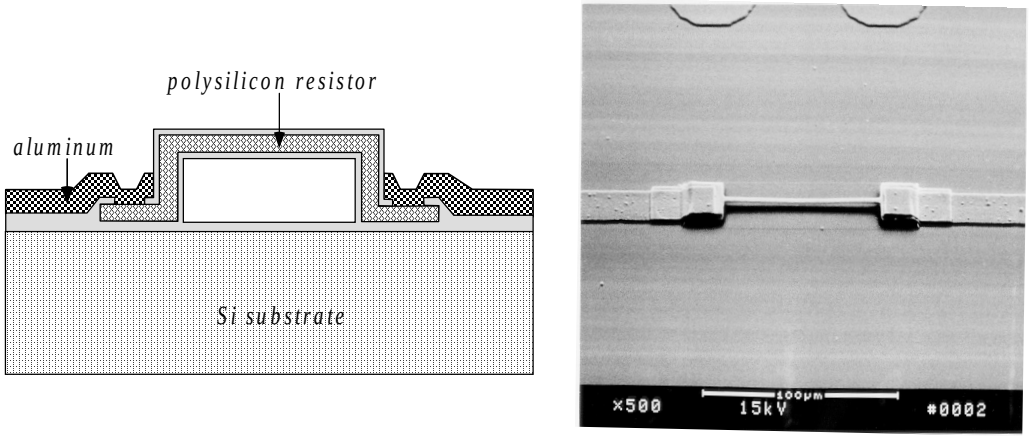

(b) Type III: bridge over substrate.

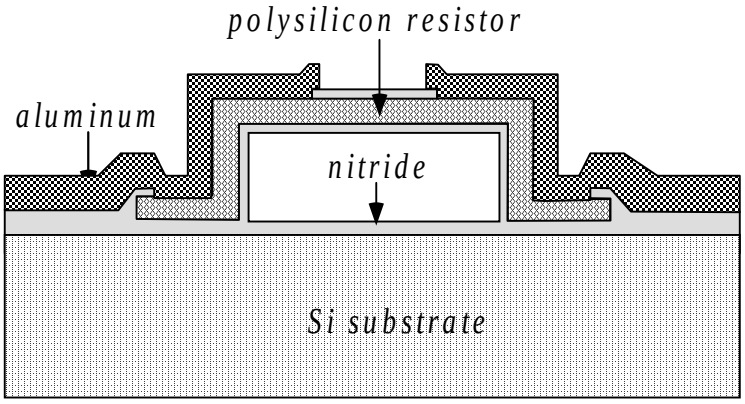

(c) Type IV: hot wire. The SEM picture is not available.

Figure 3.27 Structures and SEM pictures of other types of micromachined shear stress sensors.

3.6.1 Frequency Responses

The frequency responses of the sensors operating in constant current (CC) mode are compared in Figure 3.28. Note that for type I, the frequency response is determined mainly by the diaphragm properties such as thickness and thermal conductivity. For type III, since the ends of the wire are directly connected to the substrate which behaves as a perfect heat sink, the frequency response is solely determined by the polysilicon wire. For type II and IV, the diaphragm and the support shanks to which the polysilicon wires are connected can heat up through thermal conduction; therefore, each type has two corner frequencies, one corresponding to the diaphragm or the support shanks and the other (3 - 4 kHz) to the polysilicon wire. The effect of the second corner frequency can be greatly reduced if we increase the wire length or put aluminum over the support shanks.

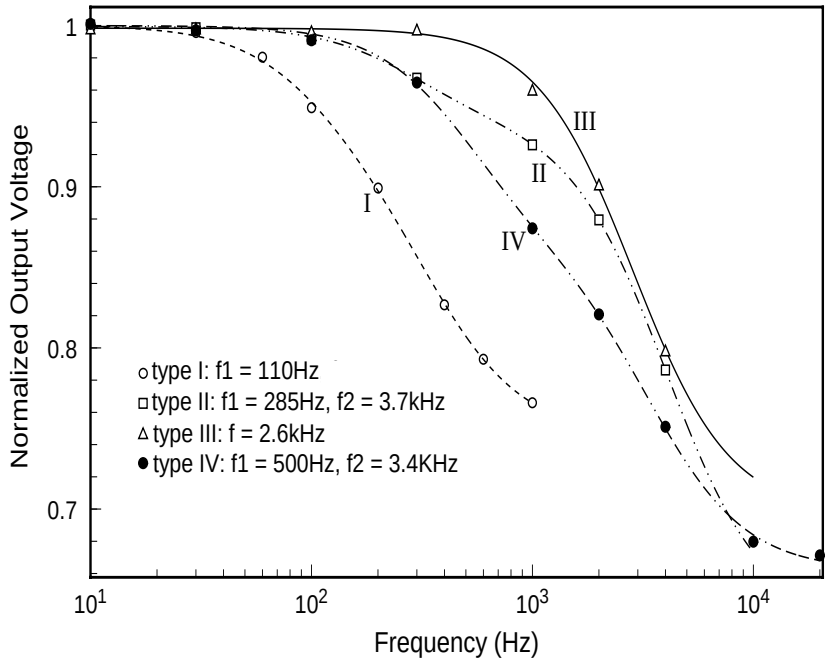

Figure 3.28 Frequency responses of four types of sensors in CC mode.

3.6.2 Thermal Resistance

To study the heat transfer characteristics, we have measured the electrical power needed to heat up the wire to a certain temperature in atmosphere and in vacuum (~ 30 mTorr) for all of the structures. The results are shown in Figure 3.29. The reciprocals of the slopes of these curves represent the thermal resistance R_{th}. Type I has the smallest thermal resistance because the nitride diaphragm is also significantly heated. The thermal resistances in atmosphere and in vacuum are not very different, meaning that most of the heat is conducted to the substrate though the diaphragm in atmosphere. Types II - IV have nearly the same thermal resistance. Their slight differences reflect different end losses. The thermal resistance in vacuum is many times smaller than that in atmosphere, meaning that in atmosphere, the end heat loss is a very small part of the total heat. The combination of the heat convection to air and heat conduction to the substrate through the air dominates the heat transfer process.

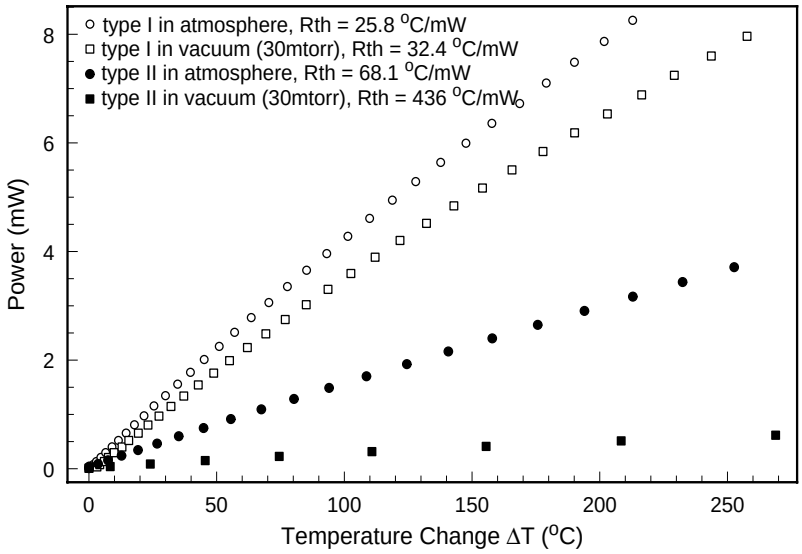

(a) Types I and II.

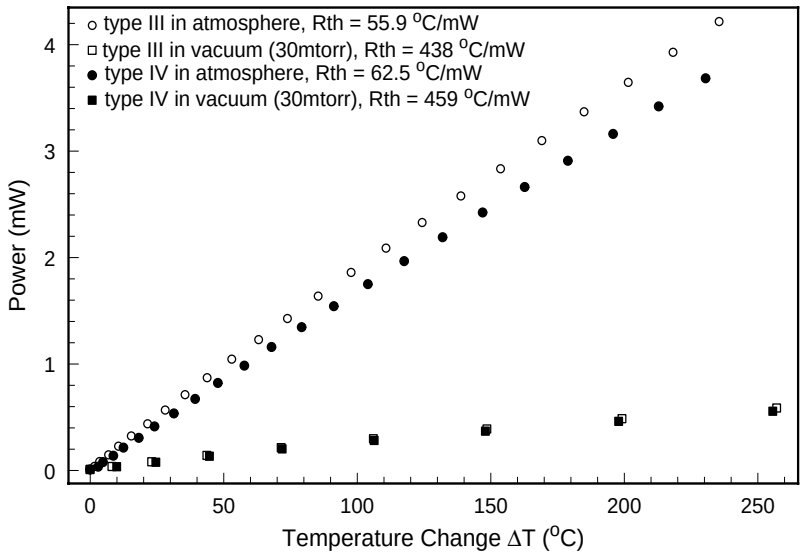

(b) Types III and IV.

Figure 3.29 Thermal resistance in atmosphere and in vacuum. The polysilicon resistors are all 120 μm long and 3 μm wide. The distance between the resistors and the substrates for types II, III and IV are 4 μm.

Another interesting test is to measure the power as a function of the height of the wire above the substrate in atmosphere for type IV sensors. This gives the information about the heat conduction loss to substrate through the air. As shown in Figure 3.30, this loss can not be neglected for *h* less than 10 μm.

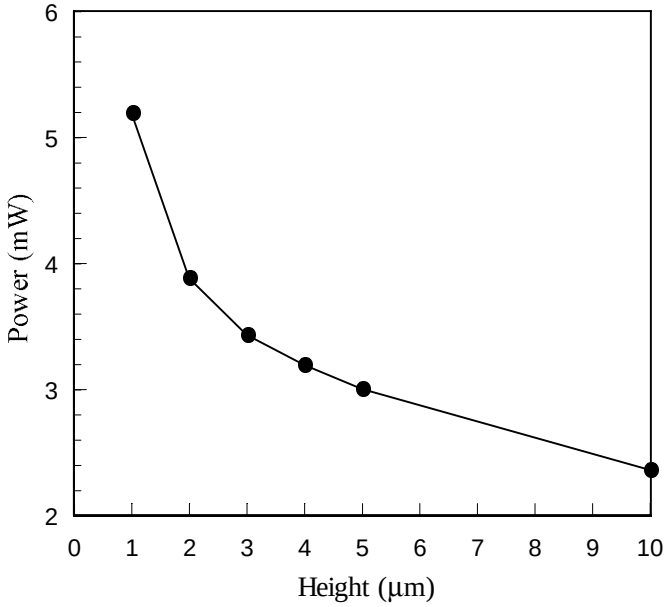

Figure 3.30 The power needed to heat up type IV sensors with different bridge height to 200^{o}C.

3.6.3 Steady-State Responses

Figure 3.31 shows the calibration results in wind-tunnel. The output changes are proportional to the one third power of shear stress, which agrees with the heat transfer theory. Types I and II are the most sensitive ones and have approximately the same relative sensitivity, despite the big difference in thermal resistance. The reason might be that when the wire is not far above the diaphragm for type II, the interaction (heat transfer) between them is almost independent of the environment change and they can be considered as a single element, just as type I sensor. Also, both type I and type II have smallest conduction loss to the substrate and are certainly more sensitive than the other two types that have significant conduction loss to the substrate through the air gaps and/or through the ends (mainly for type III). Increasing the gap height reduces the conduction loss to the substrate and improves the sensitivity for types III and IV, but then it may interfere with the flow and make the sensor more physically vulnerable.

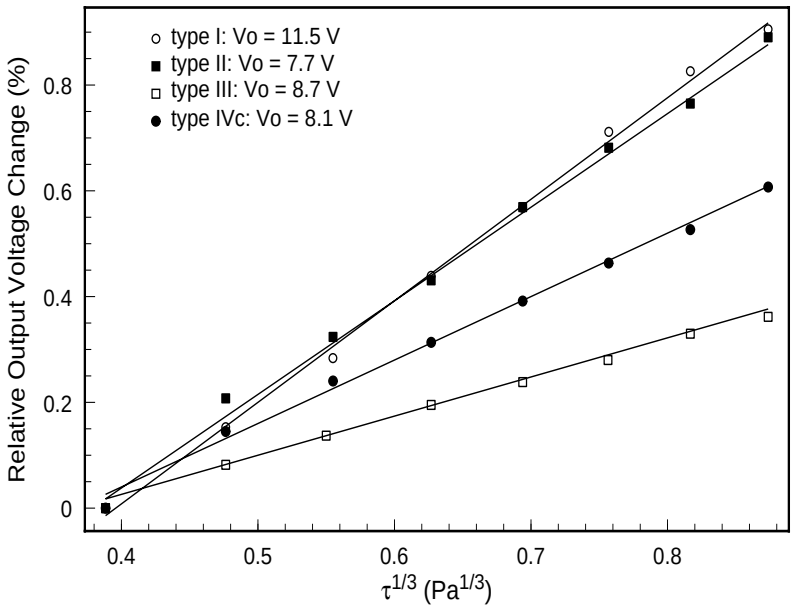

Figure 3.31 Wind tunnel calibration results for all types of micromachined shear stress sensor structures in CT mode (a_R = 0.1).

3.7 Summary

A novel MEMS thermal shear stress sensor featuring a unique vacuum cavity has been developed. The vacuum cavity dramatically improves the thermal isolation of the polysilicon sensing element from the substrate. The steady-state and transient heat transfer models of the sensor has been established and successfully used to analyze the steady-state wind-tunnel calibration results, temperature sensitivities and frequency responses. The theoretical analysis also provides the guidance for the optimization of the sensor design. Finally, other potential sensor structures are explored and their sensitivity and frequency responses are compared with the vacuum-cavity isolated sensor.

Bibliography

[1] T. J. Hanratty and J. A. Campbell, "Measurement of Wall Shear Stress," *Fluid Mechanics Measurements*, R. J. Goodstein, ed., Hemisphere Publishing, pp. 559-615, 1983.

[2] J. H. Haritonidis, "The Measurement of Wall Shear Stress," *Advances in Fluid Mechanics Measurements*, Mgad-el Hak, ed., Springer-Verlag, New York, pp. 229-261, 1989.

[3] T. E. Stanton, D. Marshall, and C. W. Bryant, "On the Condition of the Boundary of a Fluid in Turbulent Motion," *Proc. R. Soc. London A*, Vol. 97, pp. 413-434, 1920.

[4] J. H. Preston, "The Determination of Turbulent Skin Friction by Means of Pitot Tubes," *J. Roy. Aero. Scoc.*, Vol. 58, pp. 109-121, 1953.

[5] M. A. Schmidt, R. T. Howe, S. D. Senturia, and J. H. Haritonidis, "Design and Calibration of a Microfabricated Floating-Element Shear-Stress Sensor," *IEEE Tans. Electron Dev.*, Vol. ED-35, pp. 750-757, 1988.

[6] T. Pan, D. Hyman, M. Mehregany, E. Reshotko, and B. Willis, "Characterization of Microfabricated Shear Stress Sensors," *Tech. Digest 8th Int. Conf. On Solid-State Sensors and Actuators (Transducer'95)*, Stockholm, Sweden, pp.1995.

[7] A. Fage and V. M. Falkner, "On the Relation between Heat Transfer and Surface Friction for the Laminar Flow," *Aero Res. Counc. London*, R&M No.1408, 1931.

[8] H. Ludwieg, "Instrument for Measuring the Wall Shearing Stress of Turbulent Boundary Layers," NACA TM-1284, 1950.

[9] H. W. Liepmann and G. T. Skinner, "Shearing-Stress Measurements by Use of a Heated Element," NACA TN-3269, 1954.

[10] J. E. Mitchell and T. J. Hanratty, "A Study of Turbulence at a Wall Using an Electrochemical Wall-Stress Meter," *J. Fluid Mech.*, Vol. 26, pp. 199-221, 1966.

[11] B. J. Bellhouse and D. L. Schultz, “Determination of Mean and Dynamic Skin Friction, Separation and Transition in Low-Speed Flow with a Thin-Film Heated Element,” *J. Fluid Mech.*, Vol. 24, pp. 379-400, 1966.

[12] M. J. Moen and S. P. Schneider, “The Effect of Sensor Size on the Performance of Flush-Mounted Hot-Film Sensors,” *J. Fluid Eng.*, Vol. 116, pp. 273-277, 1994.

[13] W. J. McCroskey and E. J. Durbin, “Flow Angle and Shear Stress Measurements Using Heated Films and Wires,” *J. Basic Eng.*, Vol. 94, pp. 46-52, 1972.

[14] D. C. Reda, “Rise-Time Response of Nickel-Foil-on-Kapton-Substrate Hot-Film, Shear-Stress Sensors,” AIAA Paper 91-0169, 1991.

[15] B. J. Bellhouse and D. L. Schultz, “The Determination of Fluctuating Velocity in Air with a Heated Thin Film Gauges,” *J. Fluid Mech.*, Vol. 29, pp. 289-295, 1967.

[16] B. J. Bellhouse and D. L. Schultz, “The Measurement of Fluctuating Skin Friction in Air with a Heated Thin-Film Gauges,” *J. Fluid Mech.*, Vol. 32, pp. 675-680, 1968.

[17] B. W. van Oudheusden and Huising, “Integrated Flow Friction Sensor,” *Sensors & Actuators A*, Vol. 15(2), pp. 135-144, 1988.

[18] E. Kalvesten, C. Vieider, L. Lofdahl, and G. Stemme, “An Integrated Pressure-Flow Sensor for Correlation Measurements in Turbulent Gas Flows,” *Sensors & Actuators A*, Vol. 52, pp. 51-58, 1996.

[19] G. L. Brown, “Theory and Application of Heated Films for Skin Friction Measurement,” *Proc. Heat Transfer and Fluid Mechanics Institute*, Stanford University Press, pp. 361-381, 1967.

[20] P. D. Weidman and F. K. Browand, “Analysis of a Simple Circuit for Constant Temperature Anemometry,” *J. Physics E: Sci. Instrum.*, Vol. 8, pp. 553-560, 1975.

[21] I. Kidron, “Measurement of the Transfer Function of Hot-Wire and Hot-Film Turbulence Transducers,” *IEEE Tans. Instrum. & Meas.*, Vol. IM-15 (3), pp. 76-81, 1966.

[22] S. C. Ling, “Heat Transfer Characteristics of Hot-Film Sensing Element Used in Flow Measurement,” *J. Basic Engr.*, Vol. 82, pp. 629-634, 1960.

[23] F. Jiang, Y. C. Tai, J. B. Huang, and C. H. Ho, “Polysilicon Structures for Shear Stress Sensors,” *Digest IEEE TENCON’95*, Hong Kong, pp. 12-15, 1995.

[24] Y. C. Tai, R. S. Muller, “Lightly-Doped Polysilicon Bridge as Flow Meter,” *Sensors and Actuators*, Vol. 15 (1), pp. 63-75, 1988.

[25] C. H. Mastrangelo, *Thermal Applications of Microbridges*, Ph. D. Thesis, University of California at Berkeley, 1990.